Table 2. Particle Size and ζ Potential of the Micelles with Varying Folate Contents

	folate conjugation[a] (%)							
	0 (MA)	1 (FMA1)	2 (FMA2)	5 (FMA5)	10 (FMA10)	25 (FMA25)	50 (FMA50)	100 (FMA100)
particle size[b] (nm)	64.21	65.34	63.79	68.35	69.22	72.51	77.47	91.29
polydispersity index (μ/T^2)	0.1018	0.0951	0.1096	0.1232	0.1318	0.1437	0.1661	0.1973
ζ potential (mV)	−0.39	0.11	−0.67	−1.07	−1.98	−2.33	−6.95	−9.25

[a] It was determined by the mixing ratio of folate-conjugated block copolymers to the block copolymers without folate conjugation. [b] The micelles were filter-sterilized using 0.45 μm filter units (Millex-HV, Millipore, Co., Ltd., U.S.A.) prior to the measurements.

In Vitro Cytotoxicity Assay. In order to determine in vitro cytotoxicity of the micelles, a human pharyngeal cancer cell line KB was incubated with FMA, MA, and free ADR in various concentrations, changing exposure time. Exponentially growing KB cells were seeded on a 96-well culture plate (2000 cells/well) and preincubated for 24 h, followed by coincubation with the samples. After 3 and 24 h, cell culture media were replaced with fresh media, and the cells were incubated further for additional 24 h. The number of viable cells was determined by CellTiter-Glo luminescent cell viability assay (n = 8) that provides a convenient, rapid, and sensitive procedure based on quantitation of ATP, which signals the presence of metabolically active cells (*28*).

Flow Cytometric (FCM) Analysis. Cellular uptake of the micelles was analyzed by an EPICS XL Flow Cytometry Systems (Beckman Coulter, U.S.A.) monitoring autofluorescence of ADR accumulated in the cell. KB cells were seeded on a 12-well culture plate (30 000 cells/well) and preincubated for 24 h, followed by coincubation with FMA, MA, and ADR (10 mg/mL) for 3 and 24 h. The cells were then washed three times with PBS, detached by trypsinization, spun down by centrifugation, and dispersed again in PBS for FCM analysis. Data were acquired and processed with the accompanying software (*EXPO 32*).

Surface Plasmon Resonance (SPR) Analysis. Interaction between FBP and the micelles was analyzed by surface plasmon resonance (SPR) measurements using BIAcore 3000 (Biacore, Sweden). FBP was immobilized on the surface of a sensor chip (3 ng/mm^2 of FBP per channel), following the procedures provided by the manufacturer. FBP binding effects of both FMA and MA were evaluated at a flow rate of 10 μL/min with a concentration of 200 μg/mL. The micelles were allowed to flow for 30 min, and all samples were tested by replacing sensor chips on which FBPs were newly immobilized.

Pharmacological Study. Tumor-bearing mice were prepared by transplanting KB cells on the abdominal region of CD-1 nude mice (female, 6-week-old, n = 6, Charles River, Japan). When the tumor volume reached 100 mm^3, the micelles and free ADR as control were intravenously injected in a volume of 0.1 mL/10 g body weight. The drug dose was 10 mg/kg for both free ADR and the micelles (ADR equivalent). After drug injection, the blood, tumor, and major organs (heart, kidney, liver, and spleen) were collected at 0.5, 1, 3, 6, 9, and 24 h, followed by HPLC analysis as previously reported (*19*). Briefly, plasma was separated from the blood, and the tissues were homogenized prior to the measurements. Daunorubicin (DAU) was added to the specimens as an internal standard in 2 μg/mL, depending on sample amount. 200 μL of 10 mM HCl solution was then added to the specimens to cleave drug conjugation, and 1 mL of 100 mM ammonia buffer (pH 9.0) was applied after 24 h incubation. 5 mL of $CHCl_3$/MeOH (2:1) mixed solution was also added to the solution, and ADR and DAU were extracted by vigorous vortexing at 25 °C for 15 min. The organic layer was collected using Pasteur pipets and evaporated at 40 °C after centrifugation (1900 g, 15 min, 4 °C). Dry drugs were redissolved in 100 μL of DMF and injected to RPLC equipped with a μ Bondasphere 5μ C4 300 column and a fluorescence detector (Ex 485 nm, Em 560 nm). The area under the curve of concentration (AUC) vs time was calculated by the trapezoidal rule with the time points of 0.5, 1, 3, 6, 9, and 24 h. The unit for AUC is defined as % dose/mL plasma × h or % dose/g organ × h for the blood or other tissues (tumor, kidney, liver, spleen, and heart), respectively.

Table 3. Time-Dependent Increase in Cytotoxicity and Cellular Uptake of the Micelles (n = 8)[a]

sample	exposure time (h)	IC_{50}[b] (μg/mL ± SD)	relative index[c]	cellular uptake[d] (%)
ADR	3	0.069 ± 0.014	1.97	100.00
	24	0.035 ± 0.011	1	100.00
FMA100	3	0.172 ± 0.017	4.91	92.51
	24	0.041 ± 0.012	1.17	94.95
MA	3	N.D.[e]	N.D.[e]	40.20
	24	0.263 ± 0.013	7.51	82.05

[a] Data were obtained from the eight independent experiments using a human pharyngeal cancer cell KB. [b] IC_{50} means the inhibitory concentration of the drugs required for reducing 50% of cell proliferation. The drug concentration of the micelles was calculated with respect to free ADR equivalents. [c] Relative index means the ratio between the IC_{50} of free ADR after 24 h incubation and the samples. [d] Cellular uptake of the micelles was analyzed by flow cytometric analysis monitoring autofluorescence of ADR accumulated in the cell. [e] N.D. means not determined.

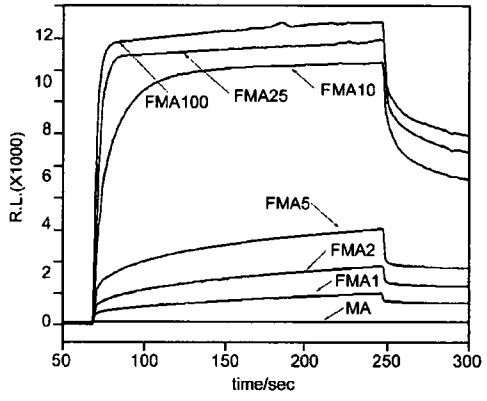

Figure 2. Surface plasmon resonance (SPR) analysis. FBP-binding selectivity of folate-conjugated micelles was evaluated by SPR measurements (eluent, 100 mM phosphate buffer; pH 7.4; flow rate, 10 mL/min; density of folate-binding protein, 3 ng/mm per channel; sample concentration, 200 μg/mL). Folate concentration on the surface of the micelles was varied to determine the optimum substitution rate.

In Vivo Antitumor Activity Evaluation. Tumor-bearing mice were prepared as described above. The micelles were injected from the tail vein three times with a four day interval in various doses (5, 10, 20, and 40 mg/kg). This administration schedule was based on the optimum regimen for free ADR as a control. However, free ADR was applied to the mice in limited doses (5, 10, and 15 mg/kg) due to the serious toxicity. Tumor growth and body weight of mice were checked at every second day. Tumor volume was calculated as volume $V = {}^1/_2 \times LW^2$, where the letters L and W denote the long and short diameters of the tumor tissue. Cancer treatment efficacy was analyzed by a treatment to control (T/C) ratio = $(V_c - V_i) \times 100/V_c$, where

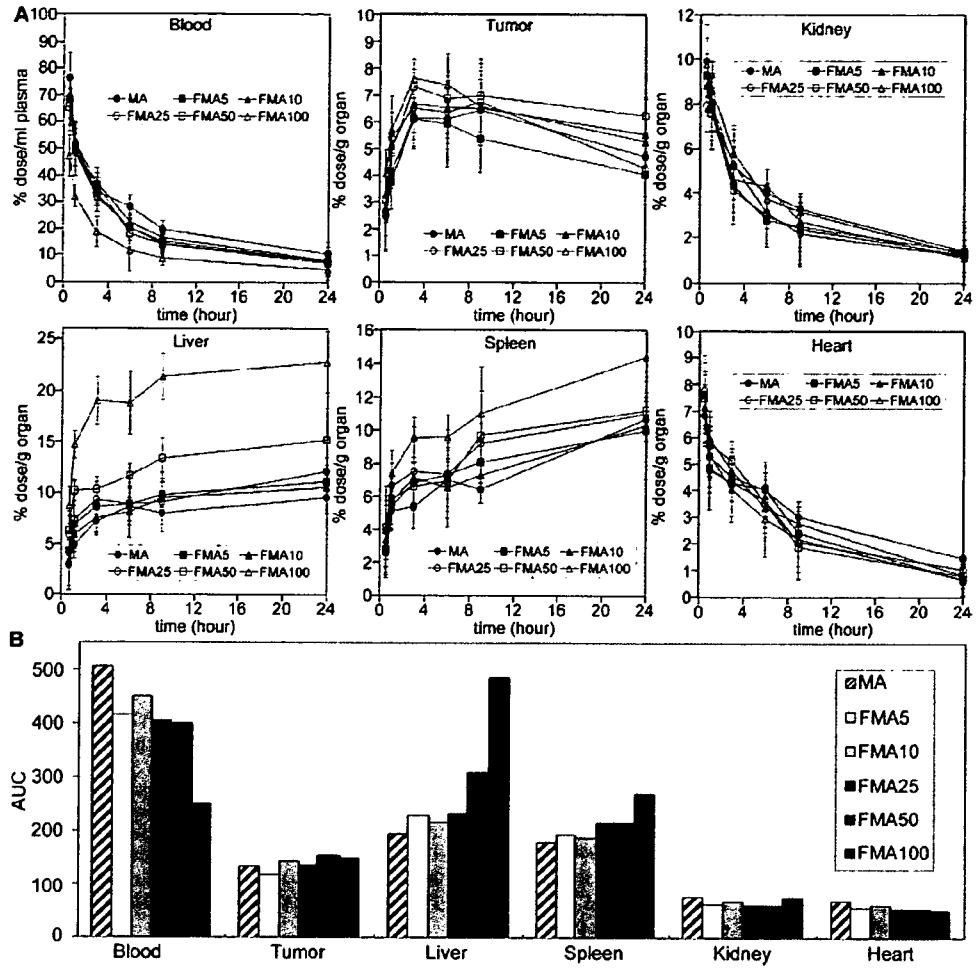

Figure 3. Pharmacokinetic profiles. Distribution of the micelles with varying folate amounts was measured in the blood compartment, tumor tissue, and major organs such as the liver, spleen, kidney, and heart (A). Experiments were carried out using tumor-bearing CD-1 nude mice (female, 6-week-old, $n = 6$) when the tumor volume reached 100 mm^3. Data are expressed as mean and mean ± SEM for relative and absolute values, respectively. Accumulation amounts for each micelle are compared in terms of the areas under the curve of concentration (AUC) vs time up to 24 h time period (B).

V_c and V_t are the mean tumor volumes of the control and the treated mice, respectively. The effective dose (ED) of each micelle was determined as the T/C ratio = 50, which means the average tumor volume of the mice decreased 50% of control values by drug treatments. The toxic dose (TD) was defined as the dose that causes 20% decrease in body weight of the mice after drug injection.

RESULTS AND DISCUSSION

Preparation of the Folate-Conjugated pH-Sensiive Polymeric Micelles (FMA). The molecular weight and composition distributions of self-assembling amphiphilic block copolymers, folate−poly(ethylene glycol)−poly(aspartate-hydrazone-adriamycin) [Fol−PEG−p(Asp-Hyd-ADR)] and α-methoxy-poly(ethylene glycol)−poly(aspartate-hydrazone-adriamycin) [PEG−p(Asp-Hyd-ADR)], were determined by GPC and ^{1}H NMR. Table 1 shows that these block copolymers were successfully prepared with a controlled number of hydrazide groups and ADR. It is noticeable that Fol−PEG−p(Asp-Hyd-ADR) block copolymers did not form any dimers or aggregates after folate conjugation. In addition, most notably, folate was functionalized only at γ-carboxylate position of its glutamate residue in this study by precision synthesis, as we previously reported elsewhere (*25*). This enables every folate molecule that is conjugated to the block copolymers to remain active, distinguishing our system from other folate conjugates. In many studies, folate molecules have been conjugated by using carbodiimide coupling reagents. The folate conjugated in this way is prone to making a mixture of α- and γ-carboxylate-functionalized forms. Because the α-carboxylate-functionalized form of folate loses its activity, the carbodiimide coupling method is substantially accompanied by the problems of undesirable introduction of inactive folate, which induces insufficient conjugation or incorrect quantification of active folate (*23, 24*). To the contrary, herein we can exclude the possibility that folate becomes inactive after conjugation, and therefore, it is able to clearly investigate the effects of folate conjugation on the biological properties of the micelles.

The particle size and ζ potential of the micelles were analyzed by Zetasizer Nano (Malvern, U.K.), and data are summarized in Table 2. Each micelle from Fol−PEG−p(Asp-Hyd-ADR) and PEG−p(Asp-Hyd-ADR) was abbreviated as FMA and MA, which denote folate micellar adriamycin and micellar adriamycin (without folate), respectively. The successive number after the abbreviated term of FMA in some descriptions indicates the mol % of Fol−PEG−p(Asp-Hyd-ADR) block copolymers in the micelles. For instance, FMA10 means that the micelles were prepared from 10% of Fol−PEG−p(Asp-Hyd-ADR) and 90% of PEG−p(Asp-Hyd-ADR) block copolymers. In all cases, the micelles exhibited particle sizes between 60 and 90 nm, while the distribution was narrow and monodisperse. Surface charge

of the micelles became negative, which is probably due to the carboxylic group remaining at the α-position of glutamate of the folate molecule. Although the micelle size slightly increased as folate concentration increased, these data demonstrate that the size and surface charge of the prepared micelles were still suitable for tumor-specific accumulation via the EPR effect after folate conjugation. When the micelle solutions were concentrated, however, aggregation between particles was observed in the case of FMA100. Such aggregation was able to be suppressed by decreasing the folate substitution ratio. Considering that MA (or FMA0) showed no aggregation during concentration, it is most probable that folate substitution increases the local concentration of folate molecules on the micelle surface, and thus, FMA aggregated due to the intermicellar hydrophobic interaction (*29*). Nevertheless, it must be noted that the micelles stably dispersed with 60−90 nm diameter up to 5 mg/mL concentration irrespective of folate substitution ratio. Because a high drug loading content (~30 wt %) is one of the characteristic advantages of the micelles, injecting the micelles above this concentration would not be realistic in terms of determining the injection dosage of ADR whose lethal dose ranges from 12.7 to 13.2 mg/kg. Therefore, it is concluded that the micelles with varying folate contents were stable at a size suitable for systemic drug delivery with sufficient drug concentration.

Folate Conjugation Significantly Increased in Vitro Cytotoxicity and Cellular Uptake of the Micelles. Table 3 shows a change in proliferation of KB cells treated by FMA100, MA, and free ADR and cellular uptake. It is of interest that the 50% inhibitory concentrations (IC_{50}) of cell growth decreased significantly in the case of the micelles by folate conjugation. Notably, cytotoxicity of FMA100 was as high as that of free ADR after 24 h incubation despite their different internalization mechanisms. In our previous studies, it is confirmed that this pH-sensitive micelle, which was designed to selectively release drugs in the intracellular region, requires relatively long exposure time sufficient for inhibiting cell growth (> 10 h). It is because the micelles are required to enter the cell first and to release drug by sensing pH so that the released drugs accumulate in cell nuclei to intercalate with DNA, inducing cell death. In comparison with MA, FMA100 showed efficient cytotoxicity with a short exposure time of 3 h. These results suggest that folate conjugation promotes the interaction between the micelles and the cell. It is generally known that KB cells overexpress folate-binding proteins (FBPs) on the cell membrane, and therefore the FBPs can take up FMA100 to the cell interior efficiently via receptor-mediated endocytosis. Such enhanced cellular uptake probably induced higher cytotoxicity of FMA100 even with short exposure time. This hypothesis was also confirmed by flow cytometric analysis. As also summarized in Table 3, cellular uptake of FMA100 increased by folate conjugation, and such an increment corresponds well with enhanced cytotoxicity. Consequently, it is confirmed that folate conjugation enhanced cytotoxicity of the micelles by increasing cellular uptake and intracellular drug concentration.

FMA Recognized Folate-Binding Proteins (FBPs) Selectively and Strongly. Although in vitro cytotoxicity assay and flow cytometric analysis have proven that high efficacy of FMA was due to the increased intracellular drug concentration, the scientific evidence that elucidates the role of folate in accelerating cellular uptake was still required. In order to confirm the interaction between FMA and folate binding proteins (FBPs), we carried out surface plasmon resonance (SPR) analysis by using a sensor chip on which FBP molecules were immobilized. It is also of great importance to verify how folate concentrations affect FBP binding properties of the micelles, so we prepared FMA with varying folate substitution rates from 100% to 0%.

Table 4. Tumor-Specific Accumulation of the Micelles

sample	blood	tumor	liver	spleen	kidney	heart
AUC[a]						
MA	506.42	132.67	194.45	179.37	76.96	69.48
FMA5	415.53	117.13	229.35	193.65	63.15	57.01
FMA10	450.38	143.60	215.97	187.98	68.45	61.79
FMA25	405.17	135.48	233.33	215.24	61.58	55.59
FMA50	400.76	155.13	308.99	216.80	60.91	54.99
FMA100	250.16	147.86	487.30	270.14	76.10	51.87
			K_b value[b]			
MA	1	0.26	0.38	0.35	0.15	0.14
FMA5	1	0.28	0.55	0.47	0.16	0.15
FMA10	1	0.32	0.48	0.42	0.16	0.15
FMA25	1	0.33	0.58	0.53	0.17	0.16
FMA50	1	0.39	0.77	0.54	0.16	0.15
FMA100	1	0.59	1.95	1.08	0.30	0.25
			tumor to organ ratio[c] (AUC_{tumor}/AUC_{organ})			
MA	–	1	0.68	0.74	1.72	1.91
FMA5	–	1	0.51	0.60	1.81	1.92
FMA10	–	1	0.66	0.76	2.04	2.12
FMA25	–	1	0.58	0.63	1.94	2.16
FMA50	–	1	0.50	0.72	2.48	2.59
FMA100	–	1	0.30	0.55	1.94	2.41

[a] AUC denotes the area under a concentration curve that is obtained from the pharmacokinetic study with time points at 0.5, 1, 3, 6, 9, and 24 h. Values were calculated on the basis of the trapezoidal rule up to 24 h after intravenous injection. The unit for AUC is defined as % dose/mL plasma × h or % dose/g organ × h for the blood or other tissues (tumor, kidney, liver, spleen, and heart), respectively. [b] K_b value is defined as $[K_b = C_{tissue}/C_{blood}]$ where C_{tissue} and C_{blood} are the drug concentrations in the tissue and the blood, respectively. Each K_b value indicates distribution of the drugs in the vascular space ($K_b < 0.1$), extracellular space ($0.1 < K_b < 0.5$), and intracellular space ($0.5 < K_b$). [c] Tumor selectivity of the micelles was determined by calculating the relative accumulated concentrations between the tumor tissues and each organ (AUC_{tumor}/AUC_{organ}).

Figure 2 shows SPR signal intensity versus time for individual micelle samples. The micelles were flowed into the sensor channel for 3 min and rinsed with fresh buffer solution. The signal change indicates that FMA binds promptly and strongly to FBP in various folate contents while MA showed no interaction with FBP. Interestingly, FMA was able to recognize FBP even with 10% folate substitution ratio. However a significant decrease was found in the FBP binding effect between FMA10 and FMA5. In the meantime, the folate substitution rates can be converted from a percent to mol wt % on the basis of the molecular weight of block copolymers and the mixing ratio. It shows that 100% folate substitution ratio corresponds to 16.9 mmol wt % for a single micelle, and FMA10 and FMA5 were calculated to contain 1.7 and 0.8 mmol % of folate molecules, respectively. Therefore, these data revealed that the micelles require only a small quantity of folate to recognize FBPs. Folate is known to have a high affinity for FBP ($K_d < 1$ nM), and such high affinity seems to provide a strong binding property of FMA (*23, 24*).

Optimum Amounts of Folate-Facilitated Tumor Targeting Properties of the Micelles with Long Blood Circulation. The information regarding the relation between the amount of folate and biodistribution of the micelles is of primary importance to determining the compositions of FMA. Such compositions should be considered to maintain the balance between passive and active tumor targeting to realize an ultimate goal of drug delivery systems. For these reasons, we have investigated the biodistribution of FMA by changing folate contents. Figure 3 shows the distribution of the micelles in the blood compartment, tumor tissues, and major organs such as the liver, spleen, kidney, and heart after the intravenous injection. The area under a concentration curve (AUC) shows that the micelles circulated

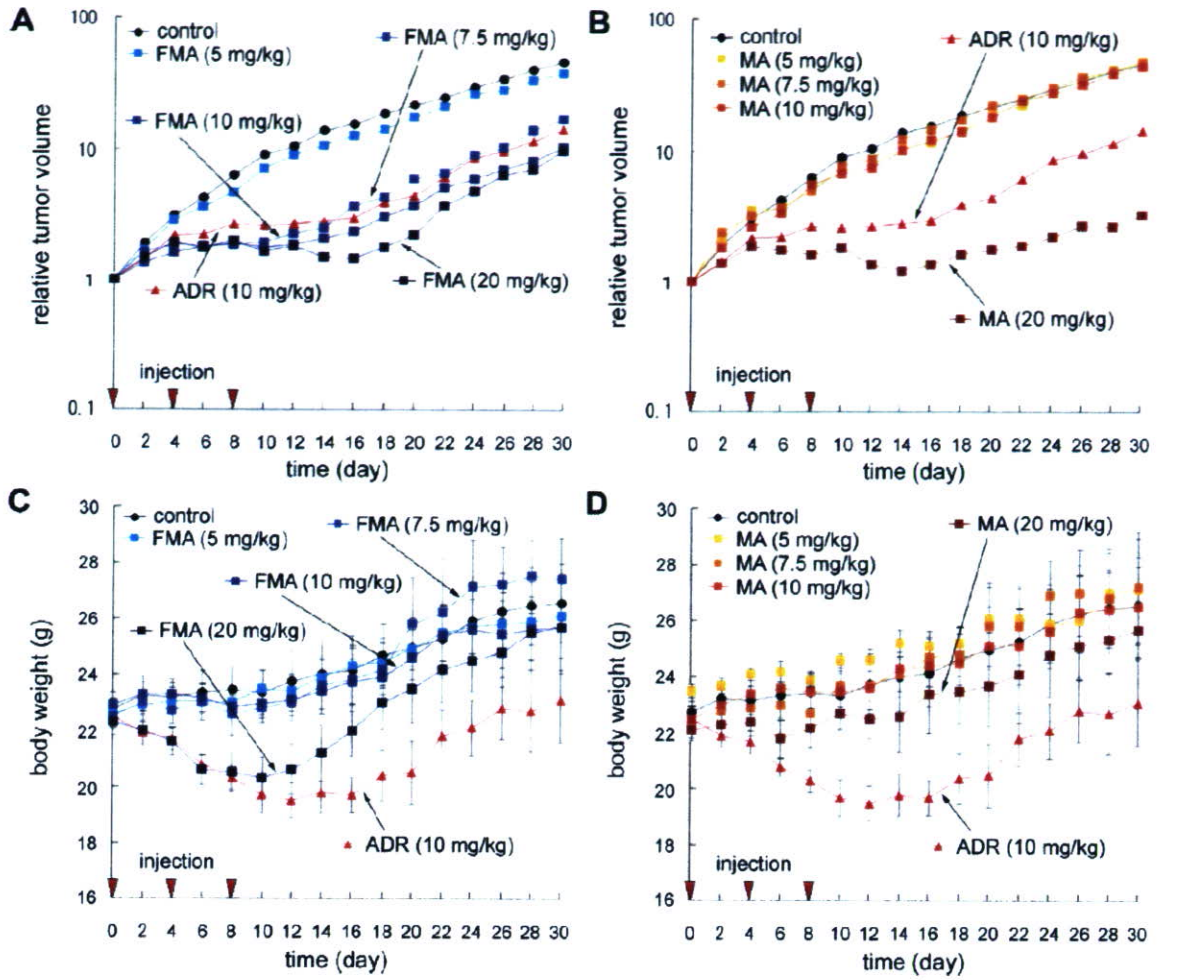

Figure 4. Tumor size and body weight change. The figure shows effective tumor-suppressing activity and low change in body weights over a broad range of injection doses of the folate-conjugated micelles (A and C). It clearly shows that the dose for effective tumor treatments decreased by folate conjugation compared to the micelles without folate, while toxicity remained lower than free drugs (B and D). Administrations were carried out 3 times with a 4 day interval into tumor-bearing CD-1 nude mice (female, 6-week-old, $n = 6$). The micelle doses are shown as ADR equivalents. Data are expressed as mean and mean ± SEM for relative and absolute values, respectively.

in the blood for a long time and their accumulation in tumor tissue increased significantly during the period of 24 h compared to normal organ. In the case of MA, the results correspond well with our previous data that revealed that the intracellular pH-sensitive micelles are characterized by prolonged circulation time in blood and tumor-specific accumulation (*19*). Such characteristic pharmacokinetic properties are considered to result from controlled drug release that can enhance the drug delivery efficiency of the micelles to the solid tumors. Regarding FMA, it is of interest that folate conjugation does not significantly affect the long-term circulation property of the micelles. FMA circulated in the blood for a prolonged time irrespective of folate content. However, the micelle accumulation in the liver as well as in the tumor changes obviously depending on the folate amount. As summarized in Table 4, a clear difference in tumor-specific accumulation was found between FMA and MA. The AUC values for each organ exhibit that FMA with a higher folate content showed a lower tumor-targeting property compared to MA. These results might be due to an increase in accumulation in the liver. Micelle accumulation in the liver was most probably due to the high FBP affinity of the micelles with increased folate concentration. In the meantime, the K_b values, which indicate the drug distribution within inter- and intracellular compartments, show that cellular uptake of FMA increased in tumor cells while remaining low in normal tissues. Nevertheless, the pharmacokinetic data also indicate that the possibility cannot be completely excluded that the micelles underwent nonspecific accumulation in normal organs after folate conjugation. It is not only because the K_b values increased, but also because the tumor to organ ratio (TOR) decreased as folate amounts increased. Accumulation in the liver increased, predominantly decreasing tumor-specific delivery efficiency. One of the previous studies showed that folate conjugation can induce higher hepatic clearance of the conjugates (*30*). Although expression of FBP in the liver would be suggested as a likely reason for the hepatic clearance, we considered that excessive conjugation of folate could increase accumulation of the micelles in normal organs. Therefore, it is concluded that the amount of folate should be carefully determined to facilitate tumor-targeting properties while maintaining long-term blood circulation. This would help us to minimize nonspecific distribution of the micelles in the body. Most noticeably, accumulation of the micelles in the tumor tissues did not significantly differ before and after folate conjugation in terms of pharmacokinetic profile. These findings indicate that the EPR effect seems to still be a major factor in determining the tumor accumulation of drug carriers for active targeting within a 24 h time range. In other words, folate conjugation would mainly affect the distribution of the micelles after extravasation rather than regulate migration of the micelles from the blood compartments to the tumor tissue.

FMA Showed Lower Toxicity and Higher Efficacy than Free Drug. The SPR analysis and biodistribution studies revealed that the optimum amount of folate conjugation is of significant importance to achieve passive and active drug targeting simultaneously. From the obtained data above, we selected FMA10 as the optimum micelle composition for further studies, which was believed to be the most suitable for the best performance in terms of tumor-specific drug delivery. In order to elucidate how folate affects in vivo antitumor activity of the micelles in detail, we have injected FMA, MA, and free ADR into the CD-1 nude mice implanted with human pharyngeal cancer KB cells by changing the dosage. Figure 4 show the changes in tumor size and body weight after drug administration. Free ADR was injected as a control, and it suppressed tumor growth at a dose of 10 mg/kg. The mice were also treated with different doses of free ADR, but there was no effect at 5 mg/kg. At a dose of 15 mg/kg, free ADR showed severe toxicity. These results indicated that free ADR was safe to exhibit the efficacy only within an extremely narrow dose range from 10 to 15 mg/kg. Indeed, body weight reduction was observed even at a dose of 10 mg/kg in the case of free ADR. In contrast to free ADR, MA was able to suppress tumor growth over a broad range of doses ranging from 20 to 40 mg/kg, while its toxicity was significantly low. Such effective and safe antitumor activity of the micelles was consistent with our previous results, which demonstrated the usefulness of intracellular pH-sensitive drug delivery (*18, 19*). Nevertheless, the effective dose (ED) of MA was relatively high compared to free ADR. In case of FMA, however, tumor growth was effectively suppressed with the same dose range of MA, but surprisingly, its ED decreased from 20 to 7.5 mg/kg while toxicity remained low. This value is even lower than the ED of free ADR (10 mg/kg), indicating that the micelles became more effective than free drug by folate conjugation. Therefore, these experimental data clearly elucidate that the drug carrier can show higher efficacy than free drug by optimally balancing passive and active tumor targeting properties as well as controlling drug release profile. It should be emphasized that, although the pharmacokinetic study showed that folate conjugation did not significantly improve the tumor-specific accumulation of the micelles, in vivo antitumor activity experiments clearly show that FMA is more effective to the cancer treatment than free ADR in terms of efficacy and safety. These results also support our hypothesis described above that active targeting seems to mainly affect the distribution profile of the drug carriers within the tumor tissues after extravasation rather than in the blood compartment. It is certain that more studies on this topic should be investigated further in the future. Nevertheless, it is of great importance that the ED of FMA decreased compared to free ADR as well as MA. A lowered dose is obviously beneficial for preventing possible long-term toxicity to the patients. From these aspects, it is concluded that our in vivo studies clearly demonstrate the effects of folate conjugation on active targeting drug delivery.

Folate Conjugation Decreased Effective Dose while Maintaining the Broad Therapeutic Window of the Micelles. The range of drug concentrations that provide the efficacy safely is known as the therapeutic window. If the injection dose is lower than this range, the drug cannot show its efficacy. To the contrary, if the injection dose is higher than the therapeutic window, the drug will induce either acute or chronic toxicity. In this study, animal studies have shown that FMA is more effective and safer than free drugs. In order to provide more objective criteria for evaluating efficacy of FMA, we analyzed antitumor activity of the micelles by calculating a treatment to control (T/C) ratio. Figure 5 exhibits the relation between the T/C ratio and a dosage. Each curve provides information about the tumor-suppressing efficacy of FMA, MA, and free ADR

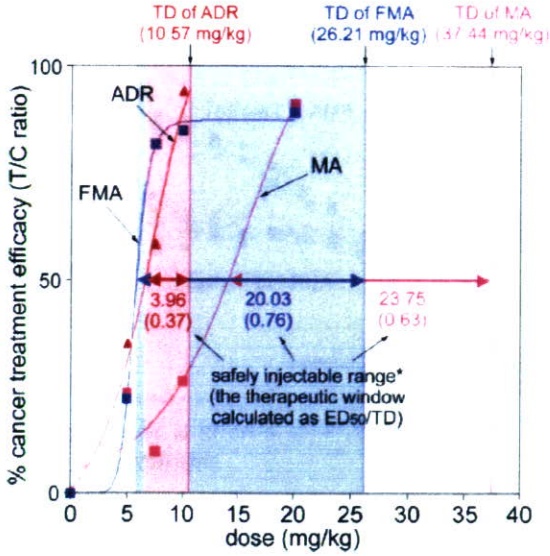

Figure 5. Treatment-to-control (T/C) ratio. Cancer treatment efficacy of the micelles was evaluated by comparing the therapeutic windows of FMA10, MA, and ADR, which were calculated from the ratio of ED_{50} to TD. ED_{50} and TD were defined as the effective dose that induces 50% decrease in tumor volume and the toxic dose that reduces 20% of body weight of mice, respectively. The data show the dose range in which each sample can be safely injected while achieving effective cancer treatments.

with respect to the control. Effective dose (ED) and toxic dose (TD) were defined as the doses that induce 50% of tumor growth (ED_{50}) and reduce 20% of body weight during the treatment, respectively. As drug concentrations increased, tumor growth suppression efficiency increased by all drug formulations. However, when we compare the effective doses, ED_{50} of free ADR is obviously close to its TD while ED_{50} of the micelles remained low compared to their TD. Namely, the safe dose of free ADR was only 3.96 mg/kg, but in contrast, FMA and MA were safely injectable between 20.03 and 23.75 mg/kg, respectively. These values correspond to 5.05- and 5.99-fold broader dose ranges than free drug. In particular, ED_{50} of FMA became lower than that of free ADR, and these results exemplify how active drug targeting is promising for cancer treatment. Most notably, such low toxicity and high efficacy were achieved by determining the optimum amount of folate on the micelle surface.

CONCLUSIONS

Integration of multiple functions into a single nanoparticle can broaden the possibilities of the macromolecular drug delivery systems for their future applications in the clinic. In this study, we have prepared a multifunctional polymeric micelle that is implemented with intracellular pH-dependent drug-releasing functionality and folate-mediated cancer cell targeting property simultaneously. By precision synthesis and preparation of the pH-sensitive micelles with varying folate contents, we were able to elucidate that the ligand-installed micelles for active drug targeting can be more effective than free drug in terms of antitumor activity, safety, pharmacokinetics, and bioavailability. It is of great interest that folate conjugation did not significantly improve the tumor accumulation of the micelles in the body because it induced a prominent increase in accumulation in the liver. However, when folate concentration was adjusted to achieve minimum ligand−receptor interaction, folate-conjugated micelles showed an effective cancer treatment efficiency that was even higher than free drugs as well as the micelles without folate conjugation. These findings clearly demonstrated that the

balance between passive and active drug targeting should be carefully considered to maximize the drug delivery efficiency as well as cytotoxic activity of the polymeric drug carriers.

ACKNOWLEDGMENT

The authors wish to express their thanks for the Project on the Materials Development for Innovative Nano-Drug Delivery Systems from the Ministry of Education, Culture, Sports, Science and Technology (MEXT), Japan.

LITERATURE CITED

(1) Duncan, R. (2006) Polymer conjugates as anticancer nanomedicines. *Nat. Rev. Cancer 6*, 688−701.

(2) Low, P. S., and Antony, A. C. (2004) Folate receptor-targeted drugs for cancer and inflammatory diseases. *Adv. Drug Delivery Rev. 56*, 1055−1058.

(3) Allen, T. M. (2002) Ligand-targeted therapeutics in anticancer therapy. *Nat. Rev. Drug Discovery 2*, 750−763.

(4) Lee, E. S., Na, K., and Bae, Y. H. (2005) Doxorubicin loaded pH-sensitive polymeric micelles for reversal of resistant MCF-7 tumor. *J. Controlled Release 103*, 405−418.

(5) Xu, Z., Gu, W., Huang, J., Sui, H., Zhou, Z., Yang, Y., Yan, Z., and Li, Y. (2005) In vitro and in vivo evaluation of actively targetable nanoparticle for paclitaxel delivery. *Int. J. Pharm. 288*, 361−368.

(6) Oyewumia, M. O., Yokela, R. A., Jaya, M., Coakleyb, T., and Mumper, R. J. (2004) Comparison of cell uptake, biodistribution, and tumor retention of folate-coated and PEG-coated gadolinium nanoparticles in tumor-bearing mice. *J. Controlled Release 95*, 613−626.

(7) Gabizon, A., Horowitz, A. T., Goren, D., Tzemach, D., Shmeeda, H., and Zalipsky, S. (2003) In vivo fate of folate-targeted polyethylene-glycol liposomes in tumor-bearing mice. *Clin. Cancer Res. 9*, 6551−6559.

(8) Jain, R. K. (1998) Delivery of molecular and cellular medicine to solid tumors. *J. Controlled Release 53*, 49−67.

(9) Matsumura, Y., and Maeda, H. (1986) A new concept for macromolecular therapeutics in cancer chemotherapy: mechanism of tumoritropic accumulation of proteins and the antitumor agent Smancs. *Cancer Res. 46*, 6387−6392.

(10) Maeda, H. (2001) SMANCS and polymer-conjugated macromolecular drugs advantages in cancer chemotherapy. *Adv. Drug Delivery Rev. 46*, 169−185.

(11) Minchinton, A. I., and Tannock, I. F. (2006) Drug penetration in solid tumours. *Nat. Rev. Cancer 6*, 583−592.

(12) Kamb, A. (2005) What's wrong with our cancer models? *Nat. Rev. Drug Discovery 4*, 161−165.

(13) Atkins, J. H., and Gershell, L. J. (2002) Selective anticancer drugs. *Nat. Rev. Cancer 1*, 645−646.

(14) Kataoka, K., Harada, A., and Nagasaki, Y. (2001) Block copolymer micelles for drug delivery: design, characterization and biological significance. *Adv. Drug Delivery Rev. 47*, 113−131.

(15) Nishiyama, N., and Kataoka, K. (2006) Nanostructured devices based on block copolymer assemblies for drug delivery: designing structures for enhanced drug function. *Adv. Polym. Sci. 193*, 67−101.

(16) Nishiyama, N., Bae, Y., Miyata, K., Fukushima, S., and Kataoka, K. (2005) Smart polymeric micelles for gene and drug delivery. *Drug Discovery Today: Technol. 2*, 21−26.

(17) Lavasanifar, A., Samuel, J., and Kwon, G. S. (2002) Poly(ethylene oxide)-block poly(L-amino acid) micelles for drug delivery. *Adv. Drug Delivery Rev. 54*, 169−190.

(18) Bae, Y., Fukushima, S., Harada, A., and Kataoka, K. (2003) Design of environment-sensitive supramolecular assemblies for intracellular drug delivery: polymeric micelles that are responsive to intracellular pH change. *Angew. Chem., Int. Ed. 42*, 4640−4643.

(19) Bae, Y., Nishiyama, N., Fukushima, S., Koyama, H., Matsumura, Y., and Kataoka, K. (2005) Preparation and biological characterization of polymeric micelle drug carriers with intracellular pH-triggered drug release property: tumor permeability, controlled subcellular drug distribution, and enhanced in vivo antitumor efficacy. *Bioconjugate Chem. 16*, 122−130.

(20) Mantovani, L. T., Miotti, S., Menard, S., Canevari, S., Raspagliesi, F., Bottini, C., Bottero, F., and Colnaghi, M. I. (1994) Folate binding protein distribution in normal tissues and biological fluids from ovarian carcinoma patients as detected by the monoclonal antibodies MOv18 and MOv19. *Eur. J. Cancer 30A*, 363−369.

(21) Weitman, S. D., Lark, R. H., Coney, L. R., Fort, D. W., Frasca, V., Zurawski, V. R., Jr., and Kamen, B. A. (1992) Distribution of the folate receptor GP38 in normal and malignant cell lines and tissues. *Cancer Res. 52*, 3396−3401.

(22) Hooijberg, J. H., de Vries, N. A., Kaspers, G. J. L., Pieters, R., Jansen, G., and Peters, G. J. (2005) Multidrug resistance proteins and folate supplementation: therapeutic implications for antifolates and other classes of drugs in cancer treatment. *Cancer Chemother. Pharmacol. 58*, 1−12.

(23) Leamon, C. P., and Reddy, J. A. (2004) Folate-targeted chemotherapy. *Adv. Drug Delivery Rev. 56*, 1127−1141.

(24) Lee, R. J., and Low, P. S. (1994) Delivery of liposomes into cultured KB cells via folate receptor-mediated endocytosis. *J. Biol. Chem. 269*, 3198−3204.

(25) Bae, Y., Jang, W.-D., Nishiyama, N., Fukushima, S., and Kataoka, K. (2005) Multifunctional polymeric micelles with folate-mediated cancer cell targeting and pH-triggered drug releasing properties for active intracellular drug delivery. *Mol. BioSyst. 1*, 242−250.

(26) Akiyama, Y., Nagasaki, Y., and Kataoka, K. (2004) Synthesis of heterotelechelic poly(ethylene glycol) derivatives having α-benzaldehyde and ω-pyridyl disulfide groups by ring opening polymerization of ethylene oxide using 4-(diethoxymethyl)benzyl alkoxide as a novel initiator. *Bioconjugate Chem. 15*, 424−427.

(27) Luo, J., Smith, M. D., Lantrip, D. A., Wang, S., and Fuchs, P. L. (1997) Efficient synthesis of pyrofolic acid and pteroyl A azide, reagents for the production of carboxyl differentiated derivatives of folic acid. *J. Am. Chem. Soc. 119*, 10004−10013.

(28) Crouch, S. P., Kozlowski, R., Slater, K. J., and Fletcher, J. (1993) The use of ATP bioluminescence as a measure of cell proliferation and cytotoxicity. *J. Immunol. Methods 160*, 81−88.

(29) Kanie, K., Nishii, M., Yasuda, T., Taki, T., Ujiieb, S., and Kato, T. (2001) Self-assembly of thermotropic liquid-crystalline folic acid derivatives: hydrogen-bonded complexes forming layers and columns. *J. Mater. Chem. 11*, 2875−2886.

(30) Shinoda, T., Takagi, A., Maeda, A., Kagatani, S., Konno, Y., and Hashida, M. (1998) In vivo fate of folate-BSA in non-tumor- and tumor-bearing mice. *J. Pharm. Sci. 87*, 1521−1526.

BC060401P

Colloidal Au Replacement Assay for Highly Sensitive Quantification of Low Molecular Weight Analytes by Surface Plasmon Resonance

Seiji Takae,[†] Yoshitsugu Akiyama,[†] Yuichi Yamasaki,[†,‡] Yukio Nagasaki,[§] and Kazunori Kataoka*[,†,‡,∥]

Department of Materials Engineering, Graduate School of Engineering, The University of Tokyo, 7-3-1 Hongo, Bunkyo-ku, Tokyo 113-8656, Japan, Center for NanoBio Integration, The University of Tokyo, 7-3-1 Hongo, Bunkyo-ku, Tokyo 113-0033, Japan, Tsukuba Research Center for Interdisciplinary Materials Science, Tsukuba University, Tennoudai 1-1-1, Tsukuba 305-8573, Japan, and Center for Disease Biology and Integrative Medicine, Graduate School of Medicine, The University of Tokyo, 7-3-1 Hongo, Bunkyo-ku, Tokyo 113-0033, Japan. Received November 9, 2006; Revised Manuscript Received April 16, 2007

A novel sensing method based on surface plasmon resonance (SPR) was developed for the highly sensitive quantification of low molecular weight (LMW) analytes (colloidal Au replacement assay). Gold nanoparticles (diameter = 20 nm) functionalized with lactosyl-poly(ethylene glycol) (PEG) were prepared and were specifically adsorbed onto a *Ricinus communis* agglutinin (RCA_{120})-immobilized SPR sensor chip surface. Subsequent injection of free D-galactose elicited the elution of the preadsorbed lactosyl-PEGylated gold nanoparticles in a manner proportional to the galactose concentration, achieving a substantial and quantitative analysis over a wide range of galactose concentrations (0.1−50 ppm). This method of D-galactose sensing through the substituted elution of preadsorbed nanoparticles from the sensor chip surface would be applicable for the highly sensitive SPR quantification of various LMW analytes, which are known to be difficult to detect by the conventional SPR sensing regime.

1. INTRODUCTION

The surface plasmon resonance (SPR) technique has been widely used in the real-time assay of biomolecular interactions (*1*−*4*). SPR is based on a change in the reflection of laser light from a metal−liquid surface, induced by a variation in the dielectric constant due to the adsorption of analyte molecules. Because this change is extremely sensitive and is correlated with the amount of adsorbed analytes, quantitative experiments with SPR are feasible for the monitoring of various biomacromolecules, including proteins, carbohydrates, and nucleic acid compounds. Nevertheless, the sensing of low molecular weight (LMW) compounds by SPR is generally difficult, mainly due to the inherently low response of analytes with a limited mass. An available method for the amplification of the SPR signal is the augmentation of the apparent mass of the analyte molecules. In this regard, gold nanoparticles modified with analytes were employed for the enhancement of the SPR signal (*5*−*7*). The amplification mechanisms of colloidal Au enhanced SPR are (i) the increased apparent mass of the analytes immobilized on gold nanoparticles and (ii) a coupling of the localized surface plasmon of gold nanoparticles with the propagating plasmon on the SPR gold surface. The colloidal Au enhanced SPR achieved the highly sensitive detection of the antigen−antibody interaction and DNA hybridization (*5*, *6*), but, as far as we know, this has not been applied to a direct quantitative assay of low molecular weight (LMW) analytes in sample solutions.

We now report a novel SPR method for the quantitative assay of LMW analytes (colloidal Au replacement assay) based on the elution of preadsorbed gold nanoparticles on the sensor chip surface induced by the injection of LMW analytes. In this method, it is crucial to minimize the nonspecific adsorption between the gold nanoparticles and the sensor chip surface. PEGylated gold nanoparticles possessing lactose moieties, as a ligand, at the distal end were then prepared by covering the nanoparticle with a densely tethered layer of a thiolated heterobifunctional PEG (*8*). Note that the hydrophilic PEG layer with a strong steric-repulsive property serves to minimize the nonspecific adsorption and agglomeration of gold nanoparticles in an aqueous medium (*9*). Eventually, the highly sensitive quantification of the label-free LMW compound, galactose, by SPR was achieved by monitoring the competitive elution of the lactosyl-PEGylated gold nanoparticles from a *Ricinus communis* agglutinin (RCA_{120}; a bivalent galactose-binding lectin)-immobilized sensor chip upon the injection of the sample solution containing a definite concentration of free galactose.

2. EXPERIMENTAL PROCEDURES

2.1. Materials. Gold nanoparticles (diameter = 20 nm) were purchased from British Biocell International (Cardiff, U.K.). Bovine serum albumin (BSA), lactosyl-albumin (lac-BSA), and NA3 glycan ($[Gal\text{-}GlcNAc]_3\text{-}Man_3\text{-}GlcNAc_2$, FW = 2006) were purchased from the Sigma-Aldrich Co. (St. Louis, MO). *Ricinus communis* agglutinin (RCA_{120}) was purchased from the Honen Co. (Tokyo, Japan). D-Galactose was purchased from Wako Pure Chemical Industries, Ltd. (Osaka, Japan). The CM3 sensor chip, acetate buffer (pH 5.5), and amine coupling kit were purchased from Biacore AB (Uppsala, Sweden). All reagents were used as received. The phosphate buffered saline (PBS, 150 mM, pH 7.4) was prepared using Dulbecco's PBS from the Dainippon-Sumitomo Pharma Co. (Osaka, Japan). Water was purified using a Milli-Q instrument (Millipore, Bedford, MA).

2.2 Preparation of PEGylated Gold Nanoparticles Possessing Varying Lactose Functionalities. PEGylated gold nanoparticles with varying lactose functionalities on the surface

* To whom correspondence should be addressed. Telephone: +81-3-5841-7138. Fax: +81-3-5841-7139. E-mail: kataoka@bmw.t.u-tokyo.ac.jp.
† Graduate School of Engineering, The University of Tokyo.
‡ Center for NanoBio Integration, The University of Tokyo.
§ Tsukuba University.
∥ Graduate School of Medicine, The University of Tokyo.

10.1021/bc0603541 CCC: $37.00
Published on Web 06/19/2007

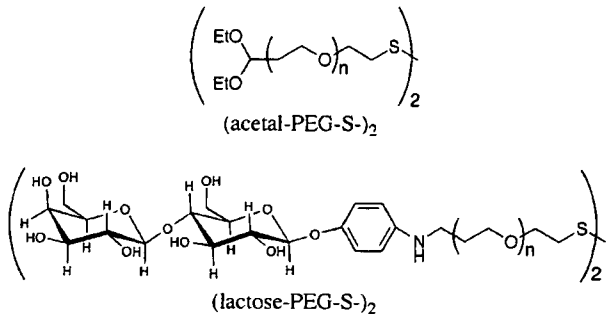

Figure 1. Chemical structures of (acetal-PEG-S-)$_2$ and (lactose-PEG-S-)$_2$.

were fabricated as previously reported (*10*). Briefly, a mixture of (acetal-PEG-S-)$_2$ (M_n = 12 100, Figure 1) and (lactose-PEG-S-)$_2$ (M_n = 12 200, Figure 1; the lactose functionality is 50%) of different molar ratios was added to the gold nanoparticle (diameter = 20 nm) solution (pH = 6.5) at room temperature. Lactose content on the gold nanoparticles was regulated by varying the feed molar ratio of (lactose-PEG-S-)$_2$ with (acetal-PEG-S-)$_2$ in the reaction mixtures. Since the reactivity of the disulfide group toward the surface of gold nanoparticles is likely to be equal between (lactose-PEG-S-)$_2$ and (acetal-PEG-S-)$_2$ because of their identical molecular weight with only a subtle change in the chain ends, the ratio of the lactose moieties on the gold surface is assumed to be equal to the feed ratio. Accordingly, the mol % of (lactose-PEG-S-)$_2$ in the feed was utilized to express the lactose functionalities (the fraction of tethered PEG having a lactosyl ligand at the distal end) on the PEGylated gold nanoparticles. Here, PEGylated gold nanoparticles with 0%, 25%, and 50% functionalities were prepared and abbreviated as lac0, lac25, and lac50, respectively. After 15 h of stirring, repetitive centrifugation and redispersion were carried out twice to remove any excess polymer from the solution. Finally, the nanoparticles were resuspended in PBS containing 0.01 wt % bovine serum albumin (BSA). The final concentration of the resuspended PEGylated gold nanoparticles was calculated from the absorbance at 523 nm using a UV−visible spectrophotometer (V-550 UV/vis spectrophotometer, JASCO, Japan). The calibration curve was prepared on the basis of the absorbance of the bare gold nanoparticles, because the UV−visible spectra revealed no substantial change even after the PEGylation of the gold nanoparticles (Supporting Information Figure S1).

2.3. Surface Plasmon Resonance Measurements. The SPR experiments were done using a Biacore 3000 instrument (Biacore AB, Uppsala, Sweden). RCA_{120} was immobilized on the surface of a CM3 carboxymethyl-dextran sensor chip using an amine coupling kit and 20 μg/mL RCA_{120} in 10 mM acetate buffer (pH 5.5) at the rate of 10 μL/min. Namely, carboxyl groups on the chip surface were activated by a mixture of succinimide (NHS) and carbodiimide (EDC) to form active esters, which then spontaneously react with the amino groups of RCA_{120}. Subsequently, excess ethanolamine was injected to deactivate the remaining active esters. The amount of the immobilized RCA_{120} was 1500 resonance units (RU) in all the experiments. A 0.1° SPR angle shift corresponds to 1000 RU, which is calibrated to be ca. 1 ng/mm^2, as provided by the manufacturer (Biacore) (*11*). Given that the molecular weight of RCA_{120} is ~120 000, it follows that 1500 RU = 1500 pg/mm^2 = 1.25×10^{-14} mol/mm^2 = 7.52×10^9 proteins/mm^2 = 7.52×10^{-3} proteins/nm^2. A similar procedure was carried out for a reference flow cell, for which the RCA_{120} injection is replaced with a blank injection of the buffer.

The lactosyl-PEGylated gold nanoparticles were then continuously injected over the flow cell modified with RCA_{120} and the unmodified flow cell at 25 °C. PBS containing 0.01 wt % BSA was used as the running buffer. All the data were obtained by signal subtraction of the blank flow cell injection from the RCA_{120}-immobilized flow cell, in order to remove any adverse contribution from the refractive index noise due to the bulk contribution of the sample injection. To assess the kinetic parameters, a global analysis of six concentrations of samples was performed using a 1:1 Langmuir model and bivalent model by *Biaevaluation 3.1* software.

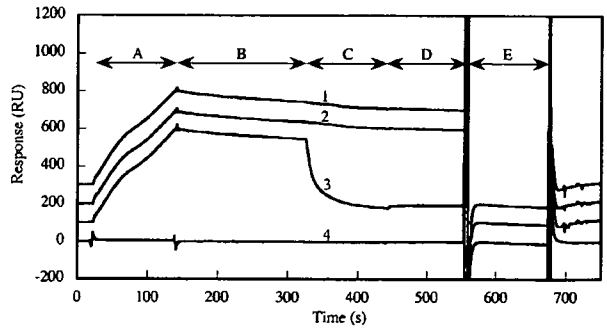

Figure 2. Sensorgrams for the interaction of PEGylated gold nanoparticles with RCA_{120} immobilized on the CM3 sensor chip. (region A): Injection of lac50 (lines 1−3) and lac0 (line 4). (region B): Flowing of running buffer (lines 1−4). (region C): Injection of running buffer (lines 1, 4), 100 μg/mL of glucose solution (line 2), and 100 μg/mL of galactose solution (line 3). (region D): Flowing of running buffer (lines 1−4). (region E): Injection of excess galactose (100 mg/mL, lines 1−4). All of these experiments were carried out at the flow rate of 5 μL/min.

2.4. Colloidal Au Replacement Assay. Lac25 and lac50 (15 nM and 5.2 nM particle concentrations, respectively) were injected over 1500 RU of an RCA_{120}-immobilized sensor chip at 10 μL/min for 5 and 3 min, respectively, producing a 900−1300 RU increase in the response. Subsequently, 0−100 ppm of galactose was injected for 5 min to elute the preadsorbed gold nanoparticles. In the elution sensorgram, the response level was normalized by the amount of the preadsorbed PEGylated gold nanoparticles (*12*, *13*). The dissociation rate constant (k_d) of the galactose-induced dissociation of lac25 and lac50 was calculated by a separate fitting against the first 15 s of the dissociation curves using a Langmuir model of the *Biaevaluation 3.1* software.

3. RESULTS AND DISCUSSION

3.1. Specificity of the Binding. Injection of lac50 (15 nM particle concentration) onto an RCA_{120}-immobilized CM3 sensor chip induced an obvious increase in the SPR signal (ca. 500 RU), in which lac0 was used as the control and conveyed low response (region A, Figure 2). The subsequent injection of 100 μg/mL galactose allowed a fast dissociation of the adsorbing lac50, whereas the same concentration of glucose did not trigger such a dissociation, and almost the same curve as the sensorgram recorded under the buffer injection was observed (region C, Figure 2), indicating the specific interaction of RCA_{120} with the lactose moieties on the PEGylated gold nanoparticles. The injection of a large excess of galactose (100 mg/mL) to the lac50-adsorbed sensor chip allowed the complete dissociation of the lac50, and eventually led to a regeneration of the sensor chip (region E, Figure 2).

3.2. SPR Response of PEGylated Gold Nanoparticles with Varying Lactose Surface Densities. Figure 3 shows the signal changes induced by the injection of the gold nanoparticles possessing various lactose densities (lac25, lac50) into a flow cell equipped with an RCA_{120}-immobilized sensor chip. Data for lac-BSA and NA3 glycan are also shown as controls. Obviously, the lactose-functionalized gold nanoparticles displayed a much higher response compared to the controls,

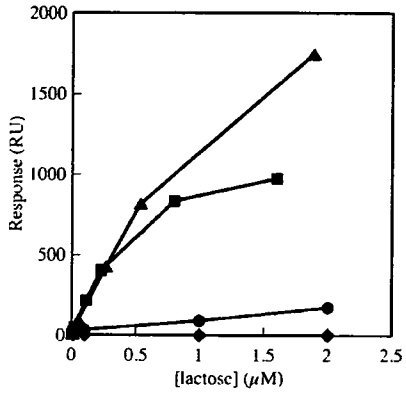

Figure 3. Binding response of various lactosylated substances onto an RCA_{120}-immobilized CM3 sensor chip (square, lac25; triangle, lac50; circle, lac-BSA; diamond, NA3 glycan). The samples were injected for 10 min at the flow rate of 5 μL/min.

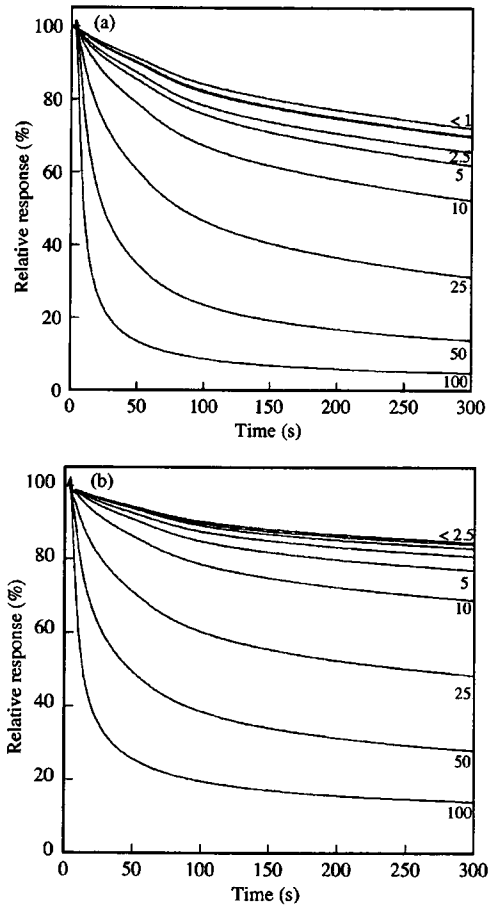

Figure 4. The elution profiles of preadsorbed lac25 (a) and lac50 (b) from an RCA_{120}-immobilized CM3 sensor chip induced by the injection of galactose. Lac25 and lac50 were injected over the sensor chip at the flow rate of 10 μL/min for 5 and 3 min, respectively. The elution of the preadsorbed nanoparticles was done by the injection of 0.1−100 ppm of galactose for 5 min. The magnitude of the net response increase from the baseline at the beginning of the elution phase was taken as 100% for each sensorgram for data normalization. The values indicated in each of the sensorgrams represent the injected galactose concentration (ppm).

indicating that the enhancement of the SPR signal based on the gold nanoparticles effectively worked. This is considered to be due to the large apparent mass and the coupling effect between the gold nanoparticles and gold surface on the sensor chip (*5*, *6*). Interestingly, the lac50 system revealed a more effective signal enhancement than the lac25 system at the same lactose concentration, even where the former has a particle concentration that is half of the latter, suggesting that the former has a higher binding affinity to the immobilized RCA_{120} than the latter.

Table 1. Kinetic Parameters for lac25-RCA_{120} and lac50-RCA_{120} Systems Determined from SPR Analysis

sample	k_a ($M^{-1}s^{-1}$)	k_d (s^{-1})	K_D (M)	χ^2
lac25	1.56×10^5	9.88×10^{-4}	6.34×10^{-9}	1.21
lac50	2.41×10^5	4.97×10^{-4}	2.06×10^{-9}	3.88

3.3. Kinetic Evaluations. To quantitatively assess the affinity of lac25 and lac50 to RCA_{120}, a kinetic analysis was carried out. A series of different concentrations of the samples was injected at the flow rate of 20 μL/min for 2 min, followed by the flowing of running buffer for 5 min to observe the dissociation phase of the samples (Figures S2 and S3). As shown in Table 1, the equilibrium dissociation constants (K_D) of the lac25-RCA_{120} and lac50-RCA_{120} systems were calculated to be 6.34×10^{-9} and 2.06×10^{-9} M, respectively, using global fitting of a Langmuir model. On the other hand, the K_D of a single lactose molecule with RCA_{120} was reported to be 3.7×10^{-3} M (*14*). It is notable that the lactosyl gold nanoparticles-RCA_{120} system has a K_D that is 6 orders smaller than the lactose-RCA_{120} system. In our previous report, lactose-installed polymeric micelles behave as a multivalent ligand for an RCA_{120}-immobilized sensor chip with a decrease in the K_D of the same order of magnitude as this system with respect to a monovalent interaction (*15*). Considering this previous report of multivalent interactions and several other references about multivalent glyconanoparticles (*16*, *17*), all of which showed that multivalency causes the nonlinear increase in the affinity, it is reasonable to also assume in this case the multivalent interactions: multiple lactose ligands on a single particle would bind with several lectin molecules on a sensor chip. In fact, in the global fitting of the sensorgrams of lac25 and lac50 using a bivalent model, a sufficiently low χ^2, a measure of the accuracy of the fitting, was obtained (1.26 and 4.03, respectively), making this fit acceptable by Biacore standards ($\chi^2 < 10$).

To gain insight into the multivalent interaction of lactose molecules on the gold nanoparticles with RCA_{120} on the sensor chip, the inter-lactose distance on the gold nanoparticles as well as the distance between two RCA_{120} molecules on the sensor chip were calculated on the basis of the following three assumptions; (i) uniform distribution of lactose molecules on the gold nanoparticles as well as of RCA_{120} molecules on the sensor chip, (ii) reduced apparent valency of an immobilized RCA_{120} molecule on the sensor chip from bivalent to monovalent against lactose molecules on the gold nanoparticles due to a steric restriction, and (iii) all of the lactose ligands accessible to the binding site of RCA_{120}, neglecting the possible decrease in the number of available lactose molecules due to the concealment of the chain end into the flexible PEG coils. As previously reported (*10*), the diameter including the PEG layer of the PEGylated gold nanoparticles was evaluated to be 33.3 nm from SEM, and the number of PEG chains on a single gold nanoparticle was estimated to be 520 chains/particle from a thermogravimetric analysis. Accordingly, the number of lactose molecules and the inter-lactose distance on lac25 and lac50 were calculated and summarized in Table 2 . Alternatively, on the basis of the RCA_{120} density described in the Experimental Section 2.3 (7.52×10^{-3} proteins/nm^2), the area occupied by a single RCA_{120} molecule on the sensor chip was calculated to be $(7.52 \times 10^{-3})^{-1} = 133$ nm^2/protein. Consequently, the average distance between RCA_{120} on the sensor chip surface is approximated to be $133^{0.5} = 11.5$ nm. It may be reasonable to then assume at least a bivalent interaction, because the inter-lactose distance on lac25 and lac50 is calculated to be less than

Table 2. Number of Lactose Molecules and Lactose Density on Gold Nanoparticles

	lac25	lac50
number of lactose molecules on a single particle[a]	130	260
area occupied by a single lactose molecule (nm^2)[b]	26.8	13.4
average distance between lactose moieties (nm)[c]	5.18	3.66

[a] Calculated from the number of PEG chains on a single gold nanoparticle (520 chains/particle) and the lactose functionality. [b] The surface area of PEGylated gold nanoparticles [$4\pi \times (33.3/2)^2$ 3.48×10^3 nm^2] was divided by the number of lactose molecules on a single gold nanoparticle. [c] Square root of the area occupied by one lactose molecule.

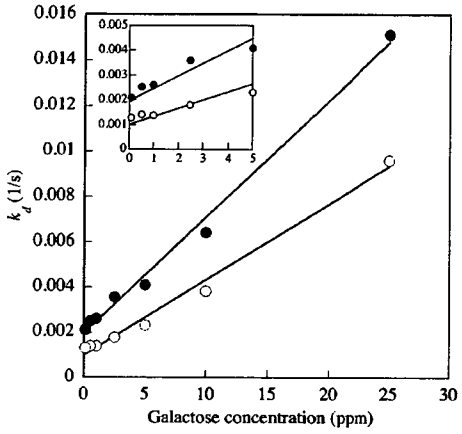

Figure 5. The relationship of the dissociation rate constant (k_d) to the injected galactose concentration. The k_d was obtained by curve fitting of the sensorgrams in Figure 4 as described in the Experimental Section. Closed circles indicate k_d of lac25 ($R^2 = 0.9924$, $\chi^2 = 3.83$), and open circles indicate k_d of lac50 ($R^2 = 0.9895$, $\chi^2 = 1.95$). The insert is the expanded figure in the range 0−5 ppm galactose.

half of the average distance between two RCA_{120} molecules on the sensor chip surface.

3.4. Colloidal Au Replacement Assay. The SPR signal enhancement by the lactosyl-PEGylated gold nanoparticles was then applied to the direct and quantitative detection of the LMW analyte, galactose. The novel method developed here (colloidal Au replacement assay) is based on the elution of the preadsorbed lactosyl-PEGylated gold nanoparticles from the sensor chip surface due to the substitution with galactose in the solution. A practical advantage of this method is that it does not require any labeling of the LMW analytes. The lactosyl-PEGylated gold nanoparticles (ca. 900−1300 RU) were initially adsorbed on the RCA_{120}-immobilized CM3 sensor chip. Free galactose, in varying concentrations (0.1−100 ppm), was then injected into the flow cell. During the elution phase of each sensorgram, the response level was normalized by the amount of the preadsorbed PEGylated gold nanoparticles as shown in Figure 4 (relative response) (*12*, *13*). Obviously, the elution of the gold nanoparticles correlated with the galactose concentration. To quantify the degree of galactose-induced dissociation, the dissociation rate constant (k_d) was calculated by curve fitting against the dissociation sensorgrams. Notably, the k_d has a linear relationship in the 0.1−25 ppm galactose concentration range for both lac25 and lac50 (Figure 5), thus permitting the quantitative analysis of galactose. Moreover, a decrease in the relative response fits nicely to a linear relationship with the galactose concentration for both lac25 (Figure 6A) and lac50 (Figure 6B) measured at several time points. As seen in the inserts of Figure 6A,B, a quantitative analysis is feasible from 0.1 to 50 ppm, indicating the significantly high sensitivity of this method. It is also noted that the linearity was valid for an appreciably wide

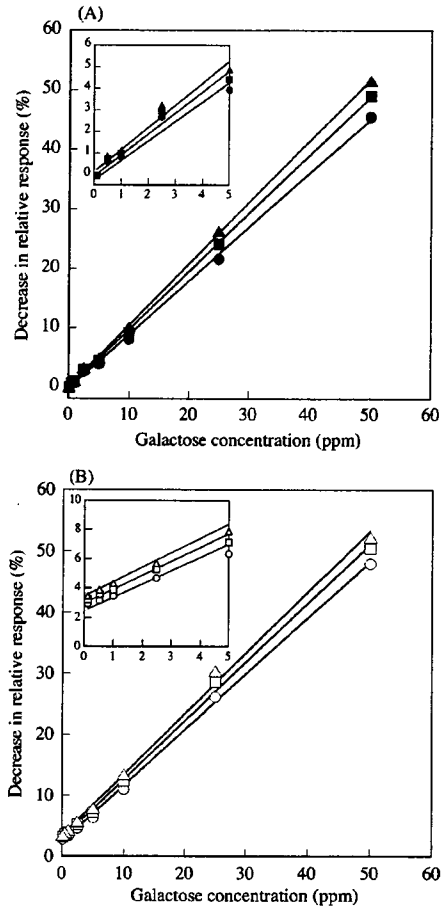

Figure 6. Relationship of the decrease in the relative response vs injected galactose concentration. All the plots in these figures were obtained by the subtraction of the relative response recorded under galactose-induced dissociation from the relative response recorded under only the running buffer. A linear response to the galactose concentration (0.1−50 ppm) was observed in all the plots ($R^2 > 0.997$). The inserts are the expanded figures in the range 0−5 ppm galactose. (A) Closed circles, squares, and triangles are the data corresponding to the time points at 25, 30, and 35 s in the sensorgrams of the lac25 elution (Figure 4a), respectively. (B) Open circles, squares, and triangles are the data points corresponding to the times of 50, 60, and 70 s in the sensorgrams of the lac50 elution (Figure 4b), respectively.

range of response times: 20−30 s for lac25 and 50−70 s for lac50. This linearity in the decrease of the relative response reveals a practical advantage of the colloidal Au replacement assay. Note that the colloidal Au replacement assay achieves a sensitivity comparable to that of ELISA in a much shorter operating time (~5 min) without any cumbersome processes of multiple washing and separation steps, which are necessary for the ELISA assay.

This method may be applicable for the quantitative sensing of various LMW compounds of practical interest, including sugars (*18*, *19*), by utilizing an appropriate combination of analyte-installed PEGylated gold nanoparticles and immobilized ligands to construct a high-throughput screening system.

4. CONCLUSION

PEGylated gold nanoparticles with different lactose functionalities (0−50%) on the distal end of PEG were prepared in order to construct a novel method for the quantitative assay of LMW analytes by SPR (colloidal Au replacement assay). The lactosyl-PEGylated gold nanoparticles showed a specific adsorption on the sensor chip surface bearing the RCA_{120} lectin,

dependent on the lactose functionality on the surface of the gold nanoparticles due to the multivalent interaction of the nanoparticles with RCA_{120} immobilized on the sensor chip. Interestingly, preadsorbed lactosyl-PEGylated gold nanoparticles on the RCA_{120}-immobilized sensor chip were eluted from the sensor chip by the injection of galactose, in a manner proportional to the galactose concentration. Eventually, this method allowed for the quantitative assay over a wide range of galactose concentrations (0.1−50 ppm) within a short operating time (~5 min). This concept of colloidal Au replacement assay would be applicable to the highly sensitive SPR quantification of various LMW analytes.

ACKNOWLEDGMENT

The authors acknowledge Dr. Eduardo Jule, the University of Tokyo, for his advice about the SPR experiments. This study was financially supported by Special Coordination Funds for Promoting Science and Technology from the Ministry of Education, Culture, Sports, Science and Technology of Japan (MEXT) as well as by the Core Research for Evolutional Science and Technology (CREST) from the Japan Science and Technology Agency (JST) and also by a Grant for the 21st Century COE Program "Human-Friendly Materials based on Chemistry" from MEXT. S.T. would like to express his special gratitude for the scholarship from the Asahi Glass Scholarship Foundation.

Supporting Information Available: Sensorgrams for the curve fitting of lac25 and lac50. This material is available free of charge via the Internet at http://pubs.acs.org/BC.

LITERATURE CITED

(1) Liedberg, B., Nylander, C., and Lundström, I. (1983) Surface plasmon resonance for gas detection and biosensing. *Biosensors and Actuators 4*, 299−304.

(2) Karlsson, R., Michaelsson, A., and Mattsson, L. (1991) Kinetic analysis of monoclonal antibody-antigen interactions with a new biosensor based analytical system. *J. Immunol. Methods 145*, 229−240.

(3) Homola, J., Yee, S. S., and Gauglitz, G. (1999) Surface plasmon resonance sensors: review. *Sens. and Actuators, B 54*, 3−15.

(4) Tawa, K., and Knoll, W. (2004) Mismatching base-pair dependence of the kinetics of DNA-DNA hybridization studied by surface plasmon fluorescence spectroscopy. *Nucleic Acids Res. 32*, 2372−2377.

(5) Lyon, L. A., Musick, M. D., and Natan, M. J. (1998) Colloidal Au-enhanced surface plasmon immunosensing. *Anal. Chem. 70*, 5177−5183.

(6) He, L., Musick, M. D., Nicewarner, S. R., Salinas, F. G., Benkovic, S. J., Natan, M. J., and Keating, C. D. (2000) Colloidal Au-enhanced surface plasmon resonance for ultrasensitive detection of DNA hybridization. *J. Am. Chem. Soc. 122*, 9071−9077.

(7) Hutter, E., Cha, S., Liu, J-F., Park, J., Yi, J., Fendler, J. H., and Roy, D. (2001) Role of substrate metal in gold nanoparticle enhanced surface plasmon resonance imaging. *J. Phys. Chem. B 105*, 8−12.

(8) Akiyama, Y., Otsuka, H., Nagasaki, Y., Kato, M., and Kataoka, K. (2000) Selective synthesis of heterobifunctional poly(ethylene glycol) derivatives containing both mercapto and acetal terminals. *Bioconjugate Chem. 11*, 947−950.

(9) Otsuka, H., Akiyama, Y., Nagasaki, Y., and Kataoka, K. (2001) Quantitative and reversible lectin-induced association of gold nanoparticles modified with α-lactosyl-ω-mercapto-poly(ethylene glycol). *J. Am. Chem. Soc. 123*, 8226−8230.

(10) Takae, S., Akiyama, Y., Otsuka, H., Nakamura, T., Nagasaki, Y., and Kataoka, K. (2005) Ligand density effect on biorecognition by PEGylated gold nanoparticles: regulated interaction of RCA_{120} lectin with lactose installed to the distal end of tethered PEG strands on gold surface. *Biomacromolecules 6*, 818−824.

(11) Stenberg, E., Persson, B., Roos, H., and Urbaniczky, C. (1991) Quantitative determination of surface concentration of protein with surface plasmon resonance using radiolabeled proteins. *J. Colloid Interface Sci. 143*, 513−526.

(12) Suzuki, F., Goto, M., Sawa, C., Ito, S., Watanabe, H., Sawada, J., and Handa, H. (1998) Functional interaction of transcription factor human GA-binding protein subunits. *J. Biol. Chem. 273*, 29302−29308.

(13) Murai, N., Taguchi, H., and Yoshida, M. (1995) Kinetic analysis of interactions between GroEL and reduced α-lactalbumin. *J. Biol. Chem. 270*, 19957−19963.

(14) Dooley, T. P., and Houston, L. L. (1982) Binding of two molecules of 4-methylumbelliferyl galactose or 4-methylumbelliferyl N-acetylgalactosamine to the B chains of ricin and ricinus communis agglutinin and to purified ricin B chain. *J. Biol. Chem. 257*, 4147−4151.

(15) Jule, E., Nagasaki, Y., and Kataoka, K. (2003) Lactose-installed poly(ethylene glycol)-poly(D,L-lactide) block copolymer micelles exhibit fast-rate binding and high affinity toward a protein bed simulating a cell surface. A surface plasmon resonance study. *Bioconjugate Chem. 14*, 177−186.

(16) Lin, C., Yeh, Y., Yang, C., Chen, G., Chen, Y., Wu, Y., and Chen, C. (2003) Quantitative analysis of multivalent interactions of carbohydrate-encapsulated gold nanoparticles with concanavalin A. *Chem. Commun.* 2920−2921.

(17) Hernaiz, M. J., de la Fuente, J. M., Barrientos, A. G., and Penades, S. (2002) A model system mimicking glycophingolipid clusters to quantify carbohydrate self-interaction by surface plasmon resonance. *Angew. Chem., Int. Ed. 41*, 1554−1557.

(18) Park, S., Boo, H., and Chung, T. D. (2006) Electrochemical non-enzymatic glucose sensors. *Anal. Chim. Acta 556*, 46−57.

(19) Perez-Olmos, R., Soto, J. C., Zarate, N., Araujo, A. N., Lima, J. L. F. C., and Saraiva, M. L. M. F. S. (2005) Application of sequential injection analysis (SIA) to food analysis. *Food Chem. 90*, 471−490.

BC0603541

Available online at www.sciencedirect.com
ScienceDirect
Journal of Controlled Release 121 (2007) 38–48
journal of controlled release
www.elsevier.com/locate/jconrel

Transfection study using multicellular tumor spheroids for screening non-viral polymeric gene vectors with low cytotoxicity and high transfection efficiencies

Muri Han [a], Younsoo Bae [b,c], Nobuhiro Nishiyama [b,c,d], Kanjiro Miyata [c,e], Makoto Oba [f], Kazunori Kataoka [a,b,c,d,e,*]

[a] Department of Materials Engineering, School of Engineering, The University of Tokyo, 7-3-1 Hongo, Bunkyo-ku, Tokyo 113-8656, Japan
[b] Center for Disease Biology and Integrative Medicine, School of Medicine, The University of Tokyo, 7-3-1 Hongo, Bunkyo-ku, Tokyo 113-0033, Japan
[c] Center for NanoBio Integration, The University of Tokyo, 7-3-1 Hongo, Bunkyo-ku, Tokyo 113-8656, Japan
[d] Core Research for Evolutional Science and Technology (CREST), Japan Science and Technology Agency (JST), Japan
[e] Department of Bioengineering, School of Engineering, The University of Tokyo, 7-3-1 Hongo, Bunkyo-ku, Tokyo 113-0033, Japan
[f] Department of Clinical Vascular Regeneration, School of Medicine, The University of Tokyo, 7-3-1 Hongo, Bunkyo-ku, Tokyo 113-8655, Japan

Received 19 March 2007; accepted 8 May 2007
Available online 17 May 2007

Abstract

Polyplexes consisting of plasmid DNA and polycations have received much attention as promising vectors for gene transfer. For effective gene therapy, polycations with different polyamine structures in the side chain were developed to ensure their buffering capacity for endosomal escape, and their PEGylated block copolymers were developed to increase their stability and biocompatibility. The effects of the chemical structures of polycations and their PEGylation on transfection and cytotoxicity were elucidated by use of a three-dimensional multicellular tumor spheroid of human hepatoma HuH-7 cells. Various features of transfection with polyplex micelles, which have been hard to observe in conventional monolayer cultures, were revealed by the multicellular tumor spheroid (MCTS) model in terms of cytotoxicity and time-dependent behaviors of transfected gene expression under three-dimensional microenvironments. By using this system, the polyplex micelle from poly(ethylene glycol)-*b*-poly(*N*-substituted asparagine) copolymers having the *N*-(2-aminoethyl)-2-aminoethyl group in the side chain (PEG-*b*-P[Asp(DET)] polyplex micelle) was proved to achieve high transfection efficiencies as well as low cytotoxicity, both of which are critical properties for successful in vivo gene delivery.

Keywords: Non-viral gene vector; Block copolymer; Polyplex micelle; Spheroid

1. Introduction

A variety of non-viral polymeric gene vectors have received much attention in the past decade [1–3] for the delivery of genetic materials to the targeted cells in an effective and safe manner. Especially, the polyplexes formed by the electrostatic interaction between plasmid DNA (pDNA) and polycations have been designed to condense pDNA by shielding its negative charges, protect pDNA from rapid nucleolytic degradation, and facilitate its cellular uptake in order to achieve effective gene delivery [4–6]. It is well known that the chemical structures of polycations in polyplex systems play important roles in transfection efficiency. In this regard, polyethylenimine (PEI)-based polyplexes have been shown to be highly transfectable, presumably through the buffering of the endosomal cavity (i.e., so-called proton sponge effect) [2]. One of the advantages of polyplex systems is the possibility of various structural modifications to improve the stability and transfection efficiency of the polyplexes. Among such modifications, PEGylation [modification with poly(ethylene glycol)(PEG)] of polycations is a promising way to realize systemic gene delivery due to the improved stability of polyplexes in biological media [7–10].

* Corresponding author. Department of Materials Engineering, Graduate School of Engineering, The University of Tokyo, 7-3-1 Hongo, Bunkyo-ku, Tokyo 113-8656, Japan. Fax: +81 3 5841 7139.
E-mail address: kataoka@bmw.t.u-tokyo.ac.jp (K. Kataoka).

0168-3659/$ - see front matter © 2007 Elsevier B.V. All rights reserved.
doi:10.1016/j.jconrel.2007.05.012

A typical PEGylated polyplex is a core-shell type polyplex (polyplex micelle) formed through the electrostatic interaction between pDNA and PEG-*block*-polycation copolymers. Polyplex micelles have been demonstrated to show high colloidal stability under biological media and substantial transfection activity against various cells even after preincubation with serum proteins [11,12]. Moreover, polyplex micelles showed prolonged blood circulation and in vivo gene transfer to liver [5,13]. The chemical structures of polycations in block copolymers substantially affect the capability of polyplexes as efficient gene vectors. In this regard, we recently reported the development of highly transfectable but remarkably low cytotoxic PEG-*block*-polycation copolymers: PEG-*b*-poly(*N*-substituted asparagine) copolymers having the *N*-(2-aminoethyl)-2-aminoethyl group in the side chain (PEG-*b*-P[Asp(DET)]) [14]. Polyplex micelles from PEG-*b*-P[Asp(DET)] showed efficient and non-toxic transfection to several primary cells including endothelial and smooth muscle cells, which are sensitive to the polyplex-induced cytotoxicity, and successful gene transfection in vivo to vascular lesions [15]. Thus, the PEG-*b*-P[Asp(DET)] polyplex micelle is expected to be a potent non-viral vector for in vivo gene delivery.

The unique feature of the PEG-*b*-P[Asp(DET)] polyplex micelle to achieve appreciably high transfection efficacy with substantially lowered toxicity motivated us to further clarify the effects of PEGylation and the chemical structures of polyasparagine-based polyplexes on their transfection and cytotoxic behaviors. For this purpose, we have compared here two types of polyasparagine-based polycations having a subtle difference in the number of methylene units in the side chain: *N*-(2-aminoethyl)-2-aminoethyl group (P[Asp(DET)]) and *N*-(3-aminopropyl)-3-aminopropyl group (P[Asp(DPT)]). Furthermore, to explore the effect of PEGylation on polyplex behavior, two types of PEG-*b*-cationic polyasparagines, PEG-*b*-P[Asp(DET)] and PEG-*b*-P[Asp(DPT)], were prepared for the construction of polyplex micelles (Scheme 1). The transfection activity and cytotoxicity of polyplexes and polyplex micelles were evaluated with multicellular tumor spheroids (MCTS) as well as conventional monolayer culture cells. We focus on MCTS here because they are known to be very useful three-dimensional in vitro tumor models, representing morphological and functional features of in vivo avascular solid tumors, and because they are characterized by prolonged viable spans with actively proliferating outer cell layers [16]. Recently, Mellor et al. applied the transfection of polyethylenimine-based polyplexes to the MCTS with the relatively large size (~474 μm) to assess the penetration of the polyplexes inside the spheroids, approaching the issue of polyplex percolation in actual in vivo tissues [17]. In the present study, we focused on the MCTS with the relatively small size due to our finding that the size of MCTS is highly sensitive to polyplex-induced cytotoxicity; MCTS of approximately 100 μm showed even higher sensitivity than monolayered culture cells, probably due to their immature development of cell–cell and cell–extracellular matrix (ECM) interactions. Worth noting is that the prolonged viable span of MCTS allowed long-term evaluation of more than 10 days of the expression of transfected genes. These properties of MCTS models enabled us to evaluate polyplex systems under conditions close to those of in vivo solid tumors, revealing the excellent biocompatibility and durable gene expression behaviors of PEG-*b*-P[Asp(DET)] polyplex micelles.

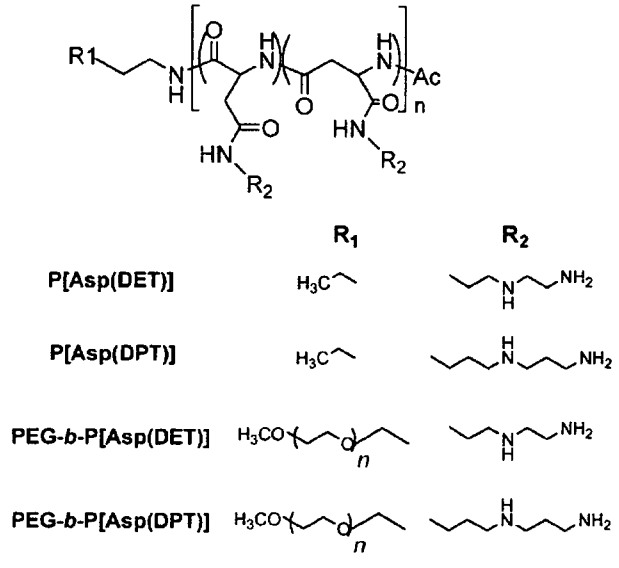

Scheme 1. Chemical structures of polycations.

2. Experimental

2.1. Materials

β-Benzyl-L-aspartate *N*-carboxyanhidride (BLA-NCA) and α-methoxy-ω-amino poly(ethylene glycol) (MeO-PEG-NH_2) (M_r=12,000) were obtained from Nippon Oil and Fats Co., Ltd. (Japan). Diethylenetriaimine (DET) and dipropylenetriamine (DPT) were purchased from Tokyo Kasei Kogyo Co., Ltd. (Japan) and distilled over CaH_2 under reduced pressure. *N,N*-Dimethylformamide (DMF), dichloromethane, and acetic anhydride were purchased from Wako Pure Chemical Industries, Ltd. (Japan) and purified by general methods before use. Linear polyethylenimine (ExGen 500 in vitro transfection reagent, 22 KDa) and branched polyethylenimine (25 KDa) were purchased from Fermentas (Canada) and Aldrich (USA), respectively.

2.2. Synthesis of poly(N-substituted asparagines) and their block copolymers with poly(ethylene glycol) (PEG)

The PEG-*block*-poly(β-benzyl L-aspartate) (PEG-*b*-PBLA) was prepared as previously reported [14]. Briefly, BLA-NCA was polymerized in DMF at 40 °C from the terminal primary amino group of MeO-PEG-NH_2, followed by the acetylation of the *N*-terminus of PBLA by acetic anhydride to obtain PEG-*b*-PBLA-Ac. PEG-*b*-PBLA-Ac was confirmed to have a unimodal molecular weight distribution (M_w/M_n: 1.17) by gel-permeation chromatography (GPC) measurement [columns: TSK-gel G4000HHR+G3000HHR, eluent: DMF+10 mM LiCl, T=40 °C, detector: Refractive Index (RI)] (data not shown).

The degree of polymerization (DP) of PBLA was calculated to be 101 based on ^{1}H NMR spectroscopy (data not shown).

Lyophilized PEG-*b*-PBLA (300 mg, 11.6 μmol) was dissolved in DMF (10 mL), followed by the reaction with DET (50 equiv to benzyl group of PBLA segment, 4.0 g, 39.4 mmol) under mild anhydrous conditions to obtain PEG-*b*-P[Asp(DET)]. After 24 h, the reaction mixture was slowly added dropwise into a solution of acetic acid (10% *v/v*, 40 mL) and dialyzed against a solution of 0.01 N HCl and then distilled water (M_r cutoff: 3500 Da). The final solution was lyophilized to obtain the polymer as the chloride salt form, and the yield was approximately 90%. Similarly, PEG-*b*-P[Asp(DPT)] was synthesized by the aminolysis reaction of PEG-*b*-PBLA-Ac with DPT. The structures of these block catiomers were confirmed by ^{1}H and ^{13}C NMR measurements.

Cationic homopolymers, P[Asp(DET)] and P[Asp(DPT)], were synthesized by the aminolysis reaction of PBLA homopolymer [degree of polymerization (DP): 98], which was obtained by the polymerization of BLA-NCA initiated by *n*-butylamine. The unimodal distribution and the almost 100% conversion of the BLA side chains of these homopolymers into the desired amino groups were confirmed by GPC and ^{1}H NMR measurements, respectively.

2.3. Titration of polymers

Each homopolymer (68 mg of P[Asp(DET)] and 75 mg of P[Asp(DPT)]) or block copolymer (98 mg of PEG-*b*-P[Asp(DET)] and 104 mg of PEG-*b*-P[Asp(DPT)]) was dissolved in 40 mL of 0.005 N HCl with 150 mM NaCl, and titrated with 0.05 N NaOH with 150 mM NaCl at 37 °C. An automatic titrator (TITSTATION TS-2000, Hiranuma Co., Ltd., Kyoto, Japan) was used for the titration. In this experiment, the titrant was added in 0.0315 mL quantities after the confirmation that the pH values became stable (minimal interval: 30 s). The pH-α curves were determined from the obtained titration curve. For the estimation of the charge in the protonation affinity with α apparent $pK(=pH+\log[\alpha/(1-\alpha)])$ was plotted against $1-\alpha$, where K is the effective dissociation constant.

2.4. Plasmid DNA

The plasmid, pCAcc vector having CAG promoter [18], was provided by RIKEN Bioresource Center (Japan). Also, a fragment cDNA of SEYFP-F46L (*Venus*), which is a variant of yellow fluorescent protein with the mutation F46L [19], was provided by Dr. A. Miyawaki at the Brain Science Institute, RIKEN (Japan) and inserted into the pCAcc vector (pCAcc+*Venus*). Each plasmid DNA (pDNA) was amplified in competent DH5α *Escherichia coli* and purified using HiSpeed Plasmid MaxiKit (QIAGEN Sciences Co., Inc., Germany). The pDNA concentration was determined by the absorption at 260 nm.

2.5. Preparation of the polyplexes

Poly(ethylene glycol)-*block*-polycation copolymer and pDNA were first separately dissolved in 10 mM Tris–HCl buffer (pH 7.4). Then, both solutions were mixed at various ratios of the number of amino group (primary and secondary amino groups) units per nucleotide (*N/P* ratios). The final pDNA concentration of the mixture was adjusted to 100 μg/mL. Polyplex micelle was applied to each well for transfection after overnight incubation at ambient temperature. Polyplex was prepared similarly by mixing cationic homopolymer and pDNA solution. Polyplex was applied to each well for transfection after 30 min of incubation at ambient temperature.

2.6. In vitro transfection to HuH-7 cells

For the monolayer culture study, human hepatoma HuH-7 cells were seeded on 24-well culture plates and incubated overnight in 400 μL of Dulbecco's modified eagle's medium (DMEM) containing 10% fetal bovine serum (FBS) before transfection. Then, 10 μL of each polyplex solution was applied to each well for the transfection. The amount of pDNA was adjusted to 1 μg per well. After 24 h of incubation, the medium was replaced with 400 μL of the medium containing 10% serum, followed by an additional 24 h of incubation. The luciferase gene expression was then evaluated using the Luciferase Assay System (Promega, USA) and a Lumat LB9507 luminometer (Berthold Technologies, Germany). The amount of protein in each well was concomitantly determined using a Micro BCA Protein Assay Reagent Kit. To prepare MCTS, 200 μL of cell suspension (2×10^2 cell/ml) was seeded into a 96-well culture plate designed for spheroid formation (SUMILONCELLTIGHT, Sumitomo Bakelite Co., Ltd., Japan). After 48 h of incubation, a multicellular spheroid with diameter of ca 100 μm was spontaneously formed in each well. Then, 10 μL of each polyplex solution was applied to each well for the transfection. The amount of pDNA was adjusted to 1 μg per well. After 24 h of incubation, the medium was replaced with 200 μL of the medium containing 10% serum, followed by an additional 24 h of incubation. During the incubation period, the medium was replaced by fresh medium containing 10% serum every 3 days. The *Venus* gene expression was then evaluated using an LSM 510 confocal microscope (Carl Zeiss, Germany; excitation wavelength: 488 nm).

2.7. Live/dead assay

Live and Dead assay was accomplished with the Live/Dead kit protocol (Molecular Probes, USA) against cultured spheroids. Spheroids were rinsed with PBS (−) and then incubated with a solution containing 0.8 μM calcein AM (excitation 495 nm, emission 515 nm) and 4 μM EthD-1 (excitation 495 nm, emission 635 nm) in PBS (−) for 3 h at 37 °C, followed by observation through a Carl Zeiss LSM 510 confocal laser scanning microscope. The concentration and incubation time were optimized to allow the selective labeling of HuH-7 spheroids between live and dead cells.

2.8. Fluorescence measurements

For observation of the gene expression of the fluorescent protein *Venus*, MCTS samples were rinsed and mounted in PBS (−), and then observed by confocal microscope. The LSM 510

laser scanning microscope was used for the optical sectioning of the spheroids. An argon gas laser with an excitation wavelength of 488 nm was used to emit the fluorescence of the YFP.

2.9. Cell viability assay

Cell viability assay was accomplished with a protocol (CellTiter-Glo®Luminescent Cell Viability Assay, Promega, USA) against cultured cells. After 24 h incubation of HuH-7 cells in opaque 24-well plates, the polyplex to be tested was added. The cells were rinsed with PBS (−) after 24 h of incubation, then 200 μL of reagent to an equal volume of cell culture medium was added to each well. After mixing for 2 min, the plate was incubated at room temperature for 10 min. The luminescence was evaluated using a Lumat LB9507 luminometer (Berthold Technologies, Germany).

2.10. Quantification of gene expression in MCTS

The total intensity was calculated from the piled up fluorescence images of fluorescence of *Venus* from each optical slice (at a depth of 1 μm) by Imaris® software in combination with Imaris MeasurementPro (Carl Zeiss, Germany), which enables the measurement of the intensity value for groups of selected voxels. The relative intensity was determined from the total intensity of one spheroid divided by a volume of spheroid.

2.11. Dissociation of P[Asp(DET)] polyplex and PEG-b-P[Asp(DET)] micelle

The release of pDNA from the complexes was evaluated through the exchange reaction with an anionic lipid, 1,2-dioleoyl-*sn*-glycero-3-phospho-L-serine sodium salt (DOPS, Sigma). Two mg/mL of DOPS solution was added to the P[Asp(DET)] polyplex and to the PEG-*b*-P[Asp(DET)] polyplex micelle solutions prepared at the *N/P* ratio of 20 to obtain mixed solutions with varying unit molar ratios ([carboxyl groups in DOPS]/[phosphate groups in pDNA]). The final pDNA concentration was adjusted to 16.7 μg/mL. After overnight incubation at 25 °C, the mixed solutions were electrophoresed with 0.9 wt.% agarose gel in the buffer (3.3 mM Tris–acetic acid (pH 7.4)+1.7 mM sodium acetate+1 mM EDTA2Na). pDNAs in the gel were visualized by soaking the gel in an ethidium bromide solution (0.5 mg/L) and analyzed using a Luminous Imager V5 (AISIN SEIKI Co., Ltd., Japan).

3. Results

3.1. Protonation behaviors of polycations and their block copolymers with PEG

In this study, sets of cationic poly(*N*-substituted asparagine) homopolymers and PEG-*b*-poly(*N*-substituted asparagine) copolymers having the *N*-(2-aminoethyl)-2-aminoethyl group (P[Asp(DET)]) or the *N*-(3-aminopropyl)-3-aminopropyl group (P[Asp(DPT)]) in the side chain (Scheme 1) were prepared to study the effects of the chemical structures of polycations as well as the PEGylation of polycations on the properties of polyplex components. This synthetic method is based on our finding that the flanking benzyl ester groups of PBLA undergo a quantitative aminolysis reaction with various polyamine compounds under careful anhydrous conditions, so that a series of polymers has the same polymerization degree and distribution [14], allowing a direct comparison of subtle changes in their chemical structures.

The pH-dependent protonation behaviors of the obtained homopolymers, P[Asp(DET)] and P[Asp(DPT)], in 150 mM NaCl-containing media at 37°C seemed to be clearly distinct as shown in Fig. 1A. Indeed, P[Asp(DET)] displayed two-step protonation behavior and the protonation degree (α) of 0.53 at pH 7.4, whereas the protonation of P[Asp(DPT)] did not show clear two-step protonation and showed a higher protonation degree (α=0.88) at pH 7.4. From the pK–α curve (data not shown), the pK_1 (pK at α=0.25) and pK_2 (pK at α=0.75) of P[Asp(DET)] were calculated as 9.1 and 6.3, respectively, and the pK_1 and pK_2 of P[Asp(DPT)] were also calculated as 9.7 and 8.6, respectively. The two distinct pK values (pK_1 and pK_2) correspond to the first and

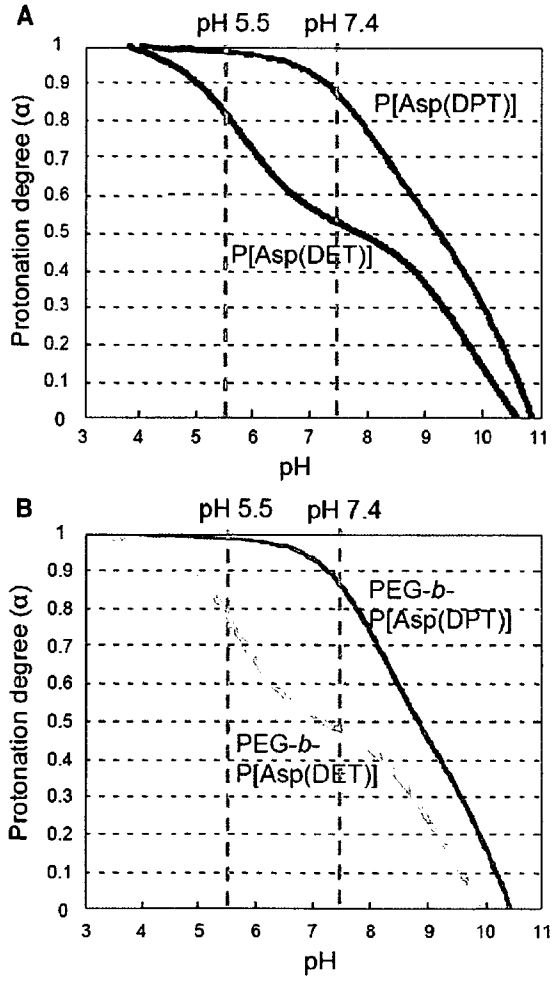

Fig. 1. pH–α (protonation degree) curves of P[Asp(DET)] and P[Asp(DPT)] (A) and PEG-*b*-P[Asp(DET)] and PEG-*b*-P[Asp(DPT)] (B) (37 °C, 150 mM NaCl, 0.05 M NaOH as titrant, 0.5 mmol amine concentration).

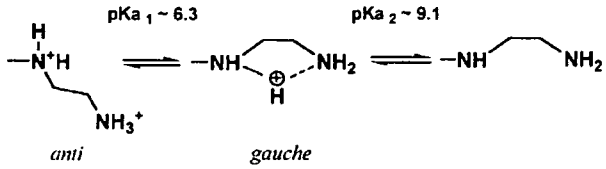

Scheme 2. Two-step protonation of ethylenediamine side chain of P[Asp(DET)].

second protonation steps of diamine units, respectively, in the side chain. Consequently, P[Asp(DET)] might exert a substantial buffering capacity in the pH range from 7.4 to 5.0, leading presumably to potent transfection activity based on the proton sponge effect. It is noteworthy that P[Asp(DET)] has a two orders of magnitude higher proton dissociation constant (or lower protonation constant) for the second protonation than P[Asp(DPT)], indicating that the former is less favorable than the latter to the double-protonated state. This may be due to the strong electrostatic repulsion between two protonated amines in ethylenediamine units of P[Asp(DET)] to take only the *anti*-conformation (Scheme 2). As seen in the case of P[Asp(DPT)], an increase in one more unit of the methylene group between two amino groups in the side chain effectively reduces the electrostatic repulsion to facilitate the protonation.

pH-α curves of PEG-*b*-poly(*N*-substituted asparagine) (PEG-*b*-P[Asp(DET)] and PEG-*b*-P[Asp(DPT)]) were also shown in Fig. 1B, showing a tendency similar to those of the homopolymers in Fig. 1A. From these results, the pK_1 and pK_2 of PEG-*b*-P[Asp(DET)] were calculated as 8.5 and 6.2, whereas the pK_1 and pK_2 of PEG-*b*-P[Asp(DPT)] were calculated as 9.3 and 8.5, respectively. It is noted that PEGylation of the polycations decreased the p*K* values, suggesting that PEGylation might prevent the protonation of polycations. Presumably, this might be explained by the decrease in the local permittivity of polycations caused by surrounding PEG chains.

3.2. Transfection efficiencies and cytotoxicity of polyplexes against monolayer cultured cells

The transfection efficiencies of cationic homopolymers/pDNA polyplexes against monolayer cultured HuH-7 cells were evaluated. The results of transfection after 48 h incubation (24 h incubation with the polyplexes followed by 24 h post-incubation after medium replacement) are shown in Fig. 2A. P[Asp(DET)] polyplexes showed high transfection efficiencies over the range of *N/P* ratios tested in this study. Especially, they displayed comparable or even higher transfection efficiencies at *N/P*=20 and 40 compared with LPEI and BPEI polyplexes [*N/P*=6 for LPEI according to the manufacturer's recommendation and *N/P*=10 for BPEI by optimization], which have been widely used in experimental transfection. P[Asp(DPT)] polyplexes showed appreciable transfection efficiency at *N/P*=10; however, the efficiency decreased at *N/P*=20 and 40, probably due to the emergence of significant cytotoxicity (Fig. 3).

Regarding the cytotoxicity of the polyplexes from cationic homopolymers (Fig. 3), both LPEI and BPEI polyplexes induced significant decreases in cell viability even at the *N/P* ratio appropriate for transfection. Polyplexes from P[Asp(DET)] were significantly less cytotoxic than the other polyplexes, whereas P[Asp(DPT)] polyplexes turned out to be highly cytotoxic. Thus, a subtle change in the chemical structure of the side chain of poly(*N*-substituted asparagine) unprecedentedly affected the cytotoxicity of the polyplexes.

In the cases of polyplex micelles from the block catiomers, PEG-*b*-P[Asp(DET)] polyplex micelles showed much better transfection efficiencies than PEG-*b*-P[Asp(DPT)] polyplex micelles (Fig. 2B), as was the case with the polyplexes from the corresponding homopolymers. With an increase in *N/P* ratio, each polyplex micelle showed an increase in transfection activity. Regarding cytotoxicity (Fig. 3), the PEG-*b*-P[Asp(DET)] polyplex micelles always displayed lower cytotoxicity than the

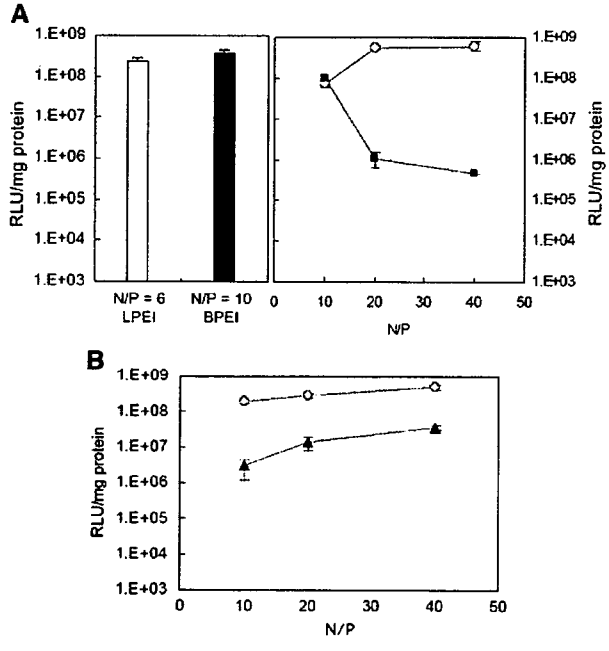

Fig. 2. The transfection of luciferase reporter gene against monolayer cultures of HuH-7. A) Transfection results with L/BPEI polyplexes (*N/P*=6 for LPEI according to the manufacturer's recommendation and *N/P*=10 for BPEI by optimization), P[Asp(DET)] polyplexes (○) and P[Asp(DPT)] polyplexes (■). B) Transfection results with PEG-*b*-P[Asp(DET)] polyplex micelles (○) and PEG-*b*-P[Asp(DPT)] polyplex micelles (▲).

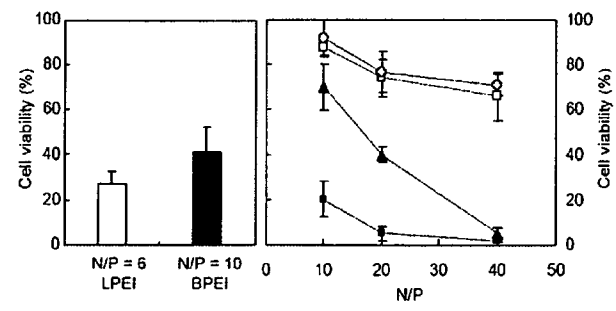

Fig. 3. Cytotoxicity of L/BPEI polyplexes (*N/P*=6 for LPEI according to the manufacturer's recommendation and *N/P*=10 for BPEI by optimization), P[Asp(DET)] polyplexes (□), P[Asp(DPT)] polyplexes (■), PEG-*b*-P[Asp(DET)] polyplex micelles (○), and PEG-*b*-P[Asp(DPT)] polyplex micelles (▲) toward HuH-7 cells after 48 h incubation.

PEG-*b*-P[Asp(DPT)] polyplex micelles at the same *N/P* ratios, and the difference in their cytotoxicity between these polyplex micelles became progressively more significant with increases in the *N/P* ratios. The cell viability remained high, and at levels similar between P[Asp(DET)] polyplexes and PEG-*b*-P[Asp (DET)] polyplex micelles, even with increased *N/P* ratios. This result suggests that the P[Asp(DET)] structure may have an inherently low cytotoxicity, which was further confirmed by the cytotoxicity assay of free polymers (Supporting Information 1). Notably, PEGylation significantly decreased the cytotoxicity of P[Asp(DPT)], resulting in improved transfection efficacy particularly at higher *N/P* ratios. This result clearly indicates that PEGylation is an efficient way to improve the compliance of a polyplex system involving cytotoxic polycations as a component [20]. Nevertheless, the PEGlyation of P[Asp(DET)] did not show any significant effect on cytotoxicity, apparently due to the minimally cytotoxic nature of the P[Asp(DET)] structure.

3.3. Evaluation of characteristic properties of MCTS

Fig. 4 shows the growth of HuH-7 MCTS from the initial diameter of 100 μm. By using Live/Dead assay (live cells: green fluorescence; dead cells: red fluorescence), necrosis of the inner cells of MCTS was observed by a confocal laser scanning microscope (CLSM) when the diameter reached around 400–500 μm (6–8 days after incubation). The necrotic region expanded along with the growth of MCTS. Thus, HuH-7 MCTS clearly took a heterogeneous structure according to the distance from the outer cell layers after they grew beyond the diffusion limit of oxygen and nutrition. Such a growth property represents a good in vitro model for the heterogeneity of solid tumors as a result of the inefficient vascular function [21,22].

3.4. Transfection efficiencies and cytotoxicity of polyplexes and polyplex micelles against MCTS

The gene expression of fluorescent protein *Venus* at defined time periods after transfection with the polyplexes or polyplex micelles was observed by CLSM as shown in Fig. 5. The spheroid diameter at the time of transfection was adjusted to 100 μm to ensure the long-term observation of the transfected gene expression within the optically observable depth range by CLSM. Under this condition, gene expression continued for over 10 days after the transfection and in some cases continued for over 1 month (data not shown). Images of the localization of transfected protein *Venus* in MCTS were taken from the upper surface going towards the center of the MCTS by the z-axis at 1–2 μm intervals of optical slices. Fig. 5A shows typical images of transfected *Venus* in MCTS at different *z*-axes (different distances from the spheroid surface) at 8 days after transfection with PEG-*b*-P[Asp(DET)] polyplex micelles (*N/P*=40). The images clearly showed that *Venus* was expressed even at the inner region of MCTS where necrosis was considered to be developed at the corresponding size (Fig. 4).

All the MCTS structures were destroyed after transfection with LPEI or BPEI polyplexes due to their toxicity even at low

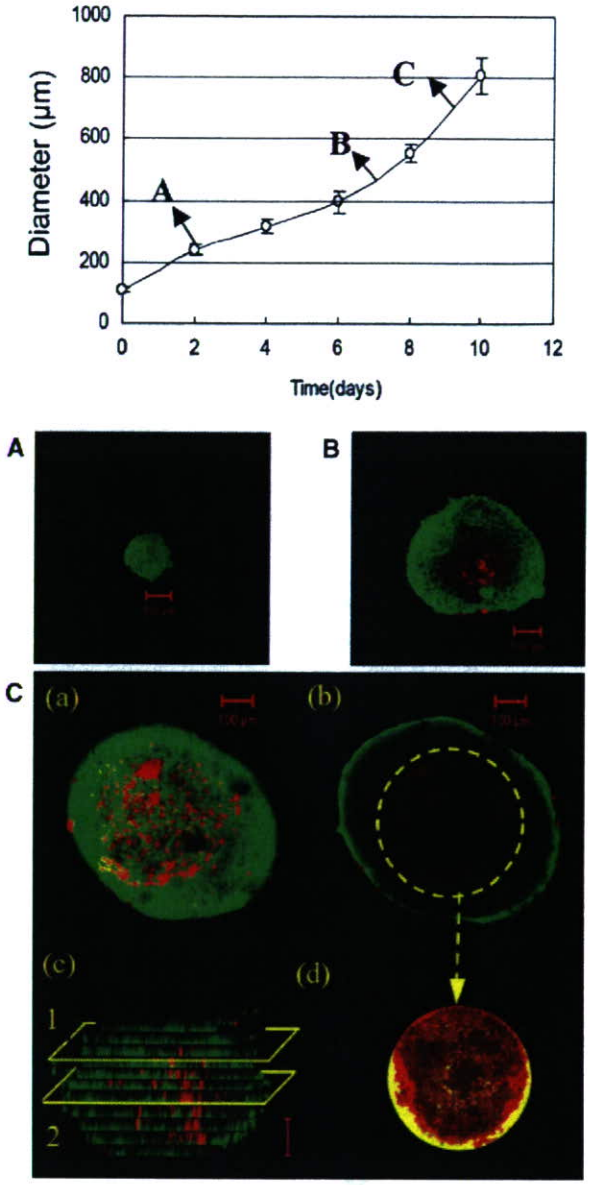

Fig. 4. Growth curve of HuH-7 spheroids and Live/Dead assay of spheroid at each time point of incubation (initial diameter is ca 100 μm. Optical slice at the middle of spheroid. Bar=100 μm. Green and red fluorescence from live and dead cells, respectively). A) 2 days after the formation of MCTS. B) 7 days after the formation of MCTS. C) 9 days after the formation of MCTS. In C, (a) optical slice of spheroid at position 1 of (c); (b) optical slice of spheroid at position 2 of (c); (c) side view of spheroid*; (d) retaken image of region of interest (ROI)**. (*This image was constructed by piling up side views. **This image was taken by stimulating the radiation of ROI by the amplification of laser.)

N/P ratios, and thus no systematic data on the spheroid transfection were obtained. P[Asp(DPT)] polyplexes also induced the destruction of MCTS in the whole range of *N/P* ratios tested in this study (*N/P*=10, 20, and 40). By contrast, P [Asp(DET)] polyplexes showed successful transfection without destruction of the MCTS structure at *N/P* ratios of 10 and 20, as seen in Fig. 5B, highlighting the lower cytotoxicity of P[Asp (DET)] compared with P[Asp(DPT)], LPEI, and BPEI. Here,

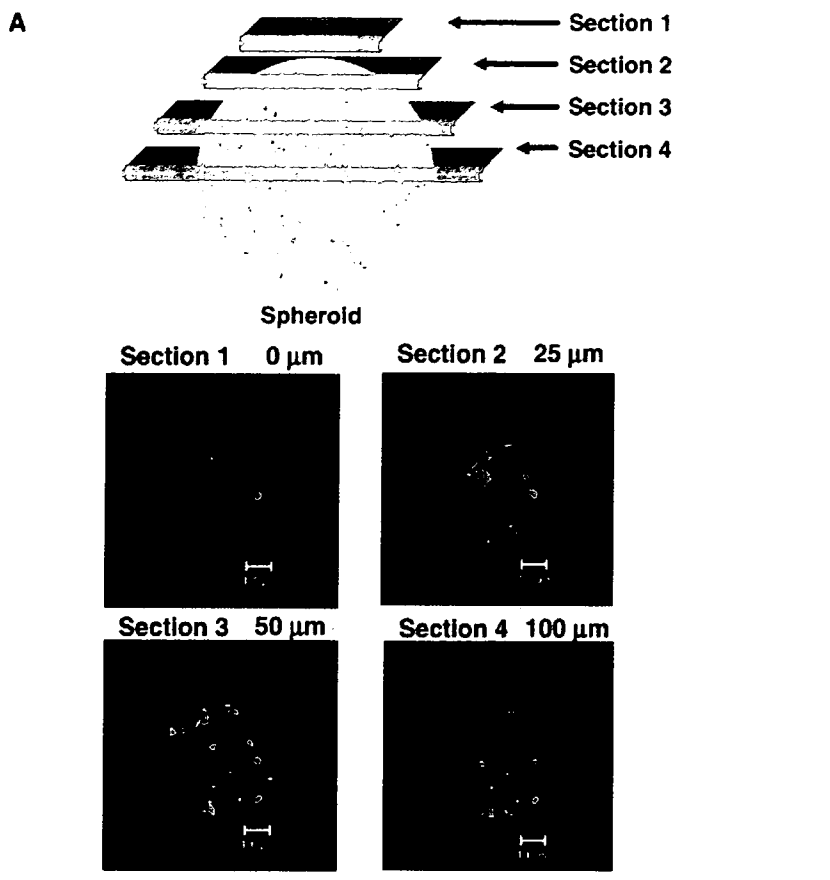
A
Section 1
Section 2
Section 3
Section 4
Spheroid
Section 1 0 μm
Section 2 25 μm
Section 3 50 μm
Section 4 100 μm

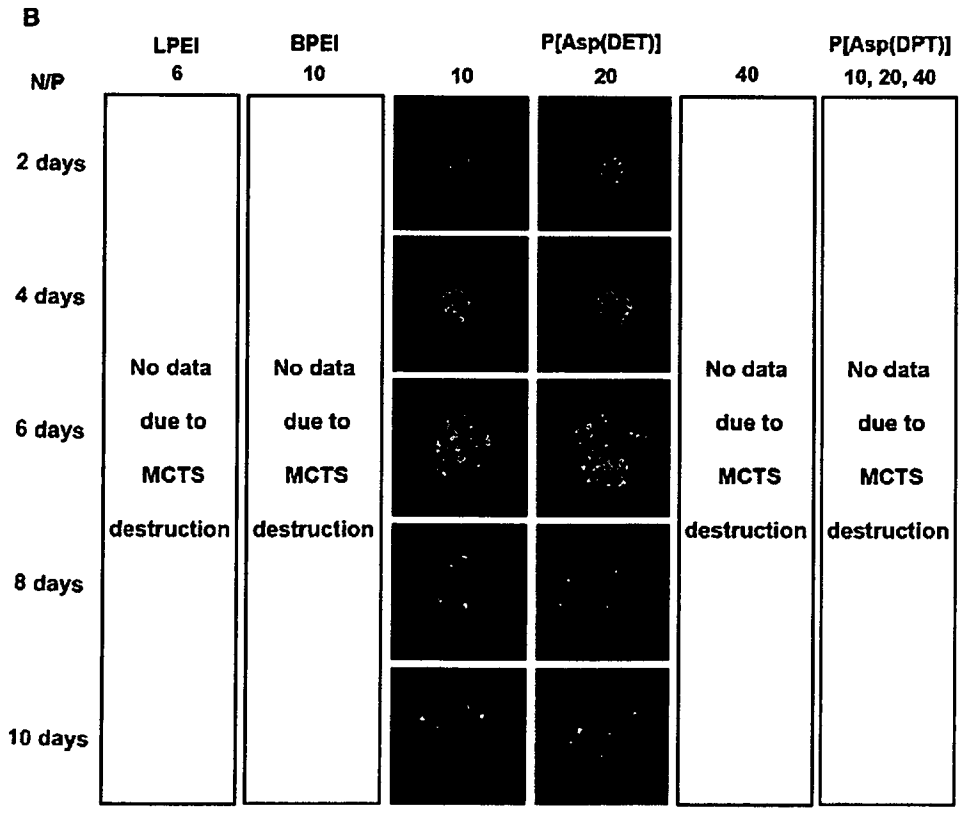
B
LPEI
BPEI
P[Asp(DET)]
P[Asp(DPT)]
N/P
6
10
10
20
40
10, 20, 40
2 days
4 days
6 days
8 days
10 days
No data due to MCTS destruction
No data due to MCTS destruction
No data due to MCTS destruction
No data due to MCTS destruction

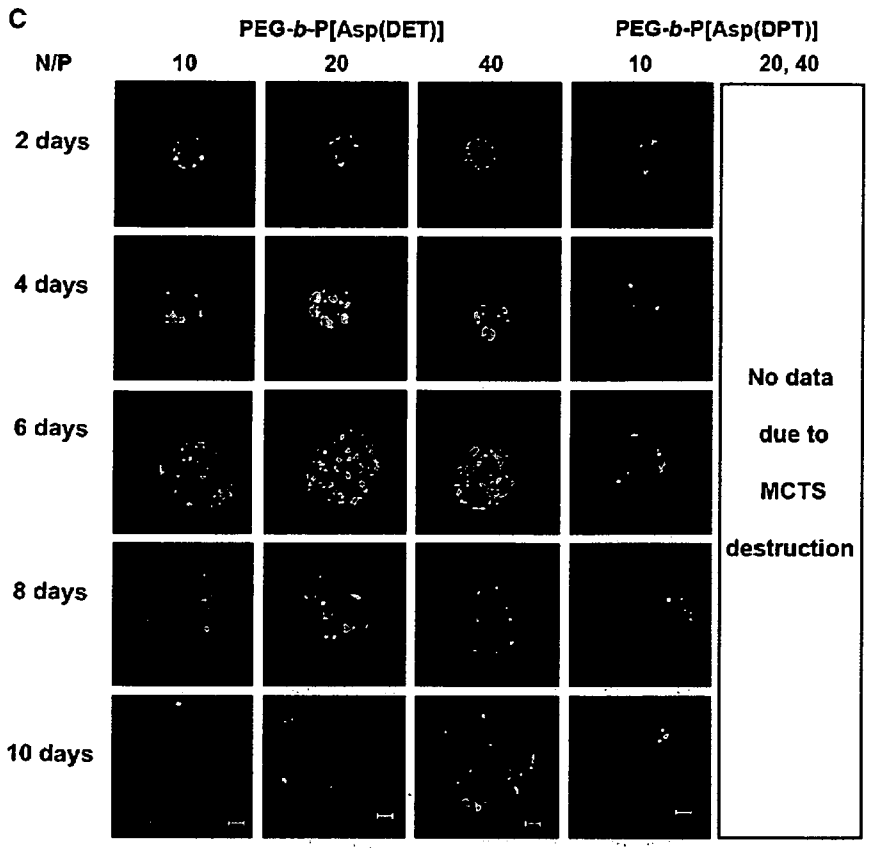

Fig. 5. Expression of marker protein *Venus* in HuH-7 spheroids (initial diameter is ca 100 μm. Bar=100 μm). A) Localization of transfected *Venus* by PEG-*b*-P[Asp(DET)] polyplex micelles according to the distance from the surface of the spheroid. (The images were the optical slices taken from the upper surface toward the center of the MCTS by the *z*-axis at 0, 25, 50, and 100 μm). B) Optical slices at the middle of spheroids with transfected protein *Venus* by P[Asp(DET)] and P[Asp(DPT)] polyplexes. (Results were not obtained due to the destruction of spheroids after transfection in the cases of $N/P=4$, 6, 8, 10 for LPEI, $N/P=10$, 20, 40 for BPEI, $N/P=40$ for P[Asp(DET)], $N/P=10$, 20, 40 for P[Asp(DPT)]). C) Optical slices at the middle of spheroids with transfected protein *Venus* by PEG-*b*-P[Asp(DET)] and PEG-*b*-P[Asp(DPT)] polyplex micelles. (Results were not obtained due to the destruction of spheroids after transfection in the cases of $N/P=20$, 40 for PEG-*b*-P[Asp(DPT)].)

the MCTS images at the middle section by the *z*-axis are shown for each day period. However, even P[Asp(DET)] polyplexes showed the destruction of spheroid structures by increasing the *N/P* ratio to 40.

Overall, PEG-*b*-P[Asp(DET) polyplex micelles showed better transfection activity than PEG-*b*-P[Asp(DPT)] polyplex micelles in MCTS, in agreement with the results of monolayer culture (Fig. 2B). PEG-*b*-P[Asp(DET)] polyplex micelles showed successful activity of the transfection without destruction of MCTS across the range of *N/P* ratios tested in this study ($N/P=10$, 20, and 40) (Fig. 5C). Worth mentioning is that PEG-*b*-P[Asp(DET)] polyplex micelles did not induce the destruction of spheroids even at $N/P=40$, where the MCTS structures were destroyed by the transfection with P[Asp(DET)] polyplexes (Fig. 5B) at that *N/P* ratio. Such reduction of cytotoxicity by PEGylation of polycations were not detected by the conventional monolayer culture study (Fig. 3, Supporting Information 1), highlighting high sensitivity of MCTS against polyplex-induced cytotoxicity. While the transfection efficiency of P[Asp(DPT)] was not obtained due to the destruction of MCTS after the transfection, the effect of PEGylation on reducing toxicity was remarkable in this case. Eventually, PEG-*b*-P[Asp(DPT)] polyplex micelles showed appreciable transfection efficiency at the *N/P* ratio of 10.

3.5. Time-dependent gene expression in MCTS

The total fluorescence intensity by *Venus* expression in MCTS was calculated by integrating the intensity image of each optical slice taken from the upper surface going towards the center of the MCTS by the *z*-axis at 1–2 μm intervals (Fig. 5A) using Imaris® software (Fig. 6A). The gene expression by the P[Asp(DET)] polyplexes ($N/P=10$ and 20) and PEG-*b*-P[Asp(DET)] polyplex micelles ($N/P=10$, 20, and 40), which showed successful transfection to MCTS, was quantified in this manner at each day period, and the results are shown in Fig. 6B. For both the polyplexes and polyplex micelles, increased the *N/P* ratios led to increased total intensities. Moreover P[Asp(DET)] polyplexes apparently had higher total intensities than PEG-*b*-P[Asp(DET)] polyplex micelles. The total intensity peaked at 6 days after transfection for all the polyplexes and polyplex micelles. It should be noted that such prolonged gene

expression is difficult to detect by the conventional monolayer culture study, because the monolayer cultured cells become confluent until 4 days, beyond which cell viability decreases remarkably. We also evaluated the relative intensity (=total intensity/volume of spheroid) of the expressed *Venus* in the spheroids transfected with the polyplexes or polyplex micelles (Fig. 6C) to normalize the differences in the growth rate and eventually the volume of each spheroid. Although the relative intensity of P[Asp(DET)] polyplexes decreased continuously with time, PEG-*b*-P[Asp(DET)] polyplex micelles with *N/P* ratios of 20 and 40 showed increased relative intensities until 4 days after transfection.

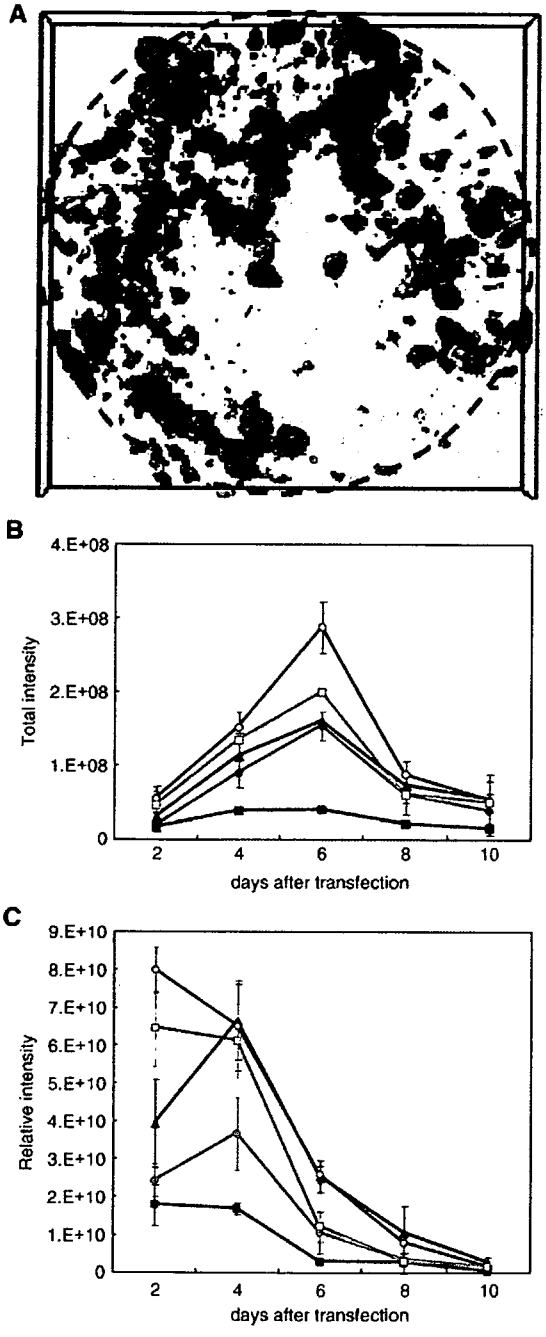

Fig. 6. Quantitative results of transfected fluorescent protein *Venus* in MCTS. A) Piled up images of transfected protein *Venus* from each slice by Imaris® (Carl Zeiss). B) Day-course of the change in total intensity by transfection with P[Asp (DET)] polyplexes (□; *N/P*=10, ○; *N/P*=20) and PEG-*b*-P[Asp(DET)] polyplex micelles (■; *N/P*=10, ●; *N/P*=20, ▲; *N/P*=40). C) Relative intensity (=total intensity/volume of spheroid) of fluorescence from transfected protein *Venus* with P [Asp(DET)] polyplexes (□; *N/P*=10, □; *N/P*=20) and PEG-*b*-P[Asp(DET)] polyplex micelles (■; *N/P*=10, ●; *N/P*=20, ▲; *N/P*=40).

3.6. DOPS-induced destabilization of P[Asp(DET)] polyplex and PEG-b-P[Asp(DET)] micelle

The differences in the time-dependency of the gene expression evaluated from the relative fluorescent intensity between P[Asp (DET)] polyplexes and PEG-*b*-P[Asp(DET)] micelles in Fig. 6C may reflect the differences in their behaviors after the internalization into the cell, because the transfection medium was replaced with fresh medium without polyplexes or micelles after 24 h. We therefore hypothesized that PEG-*b*-P[Asp(DET)] micelles may have greater stability or tolerability against pDNA unpacking, which is presumably induced through the exchange reaction with anionic components in the intracellular compartments, than P[Asp (DET)] polyplexes, thereby showing delayed gene expression. Thus, we evaluated the stability of the polyplex and polyplex micelle in the presence of anionic lipids (DOPS) as natural anionic compounds. It is known that such anionic lipids including phosphatidylserine exist appreciably in the intracellular compartments. As shown in Fig. 7, P[Asp(DET)] polyplexes (*N/P*=20) released pDNA at the [carboxyl groups in DOPS]/[phosphate groups in pDNA] (A/P) ratio of 12, whereas PEG-*b*-P[Asp(DET)] micelles (*N/P*=20) showed no pDNA release even at the highest *A/P* ratio (~17). Thus, PEG-*b*-P[Asp(DET)] micelles were judged to have higher tolerability against DOPS-induced destabilization than P[Asp(DET)] polyplexes.

4. Discussion

In this study, we prepared sets of cationic poly(*N*-substituted asparagine) homopolymers and PEG-*b*-poly(*N*-substituted asparagine) copolymers having the *N*-(2-aminoethyl)-2-aminoethyl group (P[Asp(DET)]) or *N*-(3-aminopropyl)-3-aminopropyl group (P[Asp(DPT)]) in the side chain (Scheme 1) to form polyplex-type non-viral gene vectors. To study the effects of the chemical structures of polycations and the effects of PEGylation of polycations on the properties as non-viral vectors, we carried out gene transfection to HuH-7 cells in the forms of monolayer culture and MCTS.

The in vitro evaluation of non-viral gene vectors relies mostly on the transfection study against monolayer cultured cells. However, there appear to be significant discrepancies between the environments of monolayer culture and in vivo tissues. One of these discrepancies is the short observable terms of the conventional monolayer cultures, which might prevent the study of the time-dependent properties of the gene expression of non-viral vectors. Especially for the polymeric gene delivery systems (polyplexes), in which pDNA is substantially condensed by